

## Durham Research Online

---

### Deposited in DRO:

30 January 2017

### Version of attached file:

Accepted Version

### Peer-review status of attached file:

Peer-reviewed

### Citation for published item:

Xu, S. J. and Zhang, W. G. and Gan, L. and Li, M. G. and Zhou, Y. (2017) 'Experimental study of flow around polygonal cylinders.', *Journal of fluid mechanics.*, 812 . pp. 251-278.

### Further information on publisher's website:

<https://doi.org/10.1017/jfm.2016.801>

### Publisher's copyright statement:

This article has been published in a revised form in *Journal of fluid mechanics* <https://doi.org/10.1017/jfm.2016.801>. This version is free to view and download for private research and study only. Not for re-distribution, re-sale or use in derivative works. © Cambridge University Press 2016

### Additional information:

---

### Use policy

The full-text may be used and/or reproduced, and given to third parties in any format or medium, without prior permission or charge, for personal research or study, educational, or not-for-profit purposes provided that:

- a full bibliographic reference is made to the original source
- a [link](#) is made to the metadata record in DRO
- the full-text is not changed in any way

The full-text must not be sold in any format or medium without the formal permission of the copyright holders.

Please consult the [full DRO policy](#) for further details.

# Experimental study of flow around polygon cylinders

S. J. Xu<sup>1†</sup>, W. G. Zhang<sup>2</sup>, L. Gan<sup>3‡</sup>, M. G. Li<sup>4</sup>, and Y. Zhou<sup>5</sup>

<sup>1</sup>School of Aerospace Engineering, Tsinghua University, 100084, China

<sup>2</sup>School of Aeronautics, Northwestern University, Xi'an, 710072, China

<sup>3</sup>School of Engineering and Computing Sciences, Durham University, DH1 3LE, U.K.

<sup>4</sup>Department of Mechanical Engineering, The University of Melbourne, Victoria 3010, Australia

<sup>5</sup>Institute of Turbulence-Noise-Vibration Interaction and Control, Shenzhen Graduate School, Harbin Institute of Technology, 518055, China

(Received ?; revised ?; accepted ?. - )

The wake of polygon cylinders with the side number  $N = 2 \sim \infty$  is systematically studied based on fluid force, hot-wire, Particle Image Velocimetry and flow visualisation measurements. Each cylinder is examined for two orientations, with a flat surface or a corner leading and facing normally to the free stream. The Reynolds number  $Re$  is  $1.0 \times 10^4 \sim 1.0 \times 10^5$ , based on the longitudinally projected cylinder width. The time-averaged drag coefficient  $C_D$  and fluctuating lift coefficient on these cylinders are documented, along with the characteristic properties including the Strouhal number  $St$ , flow separation point and angle  $\theta_s$ , wake width, and critical Reynolds number  $Re_c$  at which the transition from laminar to turbulence occurs. It is found that once  $N$  exceeds 12,  $Re_c$  depends on the difference between the inner diameter (tangent to the faces) and the outer diameter (connecting corners) of a polygon, the relationship being approximately given by the dependence of  $Re_c$  on the height of roughness elements for a circular cylinder. It is further found that  $C_D$  vs  $\xi$  or  $St$  vs  $\xi$  for all the tested cases collapses onto a single curve, where the angle  $\xi$  is the corrected  $\theta_s$  associated with the laterally widest point of the polygon and the separation point. Finally, the empirical correlation between  $C_D$  and  $St$  is discussed.

**Key words:** polygon cylinders, drag coefficient, Strouhal number

## 1. Introduction

Flow around bluff-bodies has attracted extensive research for more than 200 years, especially since the discovery of Kármán vortex streets. A vast number of researches have been focused on flow around stationary circular and rectangular/square cylinders; see Williamson (1996); Matsumoto (1999); Thompson *et al.* (2001); Mills *et al.* (2003); Zdravkovich (1997) among others. In addition to the important governing parameter Reynolds number  $Re$ , special attentions were usually paid to the Strouhal number  $St$ , drag coefficient  $C_D$  and fluctuating lift coefficient  $C'_L$ , which are closely associated with the vortex shedding dynamics.

Roshko (1955) discovered for the first time that, as  $C_D$  increases,  $St$  decreases and this relation is particularly pronounced after the boundary layer transition (hereafter the

† Email address for correspondence: xu\_shengjin@tsinghua.edu.cn

‡ Email address for correspondence: lian.gan@durham.ac.uk

transition). He also found that the vortex shedding frequency is related to the wake width (distance between the free streamlines separating the wake and the distorted potential outer flow, denoted as  $D_w$ ), instead of the physical width of the bluff body ( $D$ ) and proposed a wake Strouhal number  $St^R$  (also called the universal Strouhal number), viz.

$$St^R = \frac{f_s D_w}{U_s}, \quad (1.1)$$

where  $f_s$  is the vortex shedding frequency,  $U_s$  is the free stream velocity outside the boundary layer at the separation point, which is also the velocity at which the shed vortices are swept downstream. Gerrard (1966) proposed another Strouhal number, viz.

$$St^G = f_w l_f / U_\infty, \quad (1.2)$$

where  $f_w$  is the fundamental wake frequency,  $l_f$  is the vortex formation length and  $U_\infty$  is the free-stream velocity. He also discussed the importance of the diffusion length, which is the transverse thickness of the shear layer at the end of the vortex formation region. Williamson (1988) proposed a relation between the universal  $St$  and  $Re$  for laminar vortex shedding from a circular cylinder, and Ponta (2006) further discussed the influence of the shear layer thickness on this relation. Norberg (2003) summarised previous measurement methods and conducted new measurements of  $C'_L$ . He suggested a mathematical relation between  $C'_L$  and  $Re$ , and pointed out a fundamental change in the mode of vortex shedding (high- and low-quality mode of turbulent shedding, respectively) before the subcritical regime ( $5.0 \times 10^3 \lesssim Re \lesssim 8.0 \times 10^3$ ), where  $Re \equiv U_\infty D / \nu$  ( $\nu$  is the kinematic viscosity).

Since the work of Roshko (1955), a number of researchers have tried to establish more accurate or robust relations between  $C_D$  and  $St$ . For example, Hoerner (1965) proposed an empirical relation  $0.21 = C_D^{0.75} St$  applicable for  $Re > 10^3$  and for two-dimensional bodies like flat plates, aerofoils and cylinders. Bearman (1967) showed that the product  $C_D St$  only depends on  $\sqrt{1 - (C_p)_b}$ , where  $(C_p)_b$  is the base pressure coefficient. Yeung (2010) also established a relation between  $C_D St$  and  $\sqrt{1 - (C_p)_b}$  from data of an inclined flat plate, a rectangular section, a circular cylinder and a  $90^\circ$  wedge. Based on the conservation of mass, momentum and energy, Ahlborn *et al.* (2002) proposed a phenomenological model for the vortex-shedding process behind cylindrical bodies. They obtained a relation between  $St$ ,  $Re$ ,  $C_D$  and geometric wake parameters through the definition of a universal  $St$  based on the size of an individual shed vortex. Alam & Zhou (2008) conducted a theoretical analysis based on the conservation of the averaged kinetic energy given no energy exchange between the bluff body and its support. They showed on the basis of experimental data reported in the literature as well as theirs that the product  $C_D St$  is approximately a constant, which is almost independent on the shape of a bluff body, its angle of attack and  $Re$ .

Polygon cross-sectional slender cylinders with a finite number of sides  $N \geq 3$  are commonly seen in engineering problems, e.g. skyscrapers, floating tunnels, prototype supporting frames in wind tunnel tests. Similar to a circular cylinder ( $N = \infty$ ), flow around a polygon cylinder is characterised by the instability of the boundary layer, laminar-turbulent transition, separation, unsteady vortex shedding etc. Unfortunately, in contrast to the vast number of papers published on the circular cylinder wake, there has been little attention in the literature paid to the fluid dynamics of the polygon cylinder with  $N > 4$  in cross flow, and the relative data are scarce. Whenever an engineering problem related to the polygon cylinder is encountered, a usual approach is to use the data of circular or square cylinders, which are well documented, as approximations. In some circumstances, however, such an approach can be very risky since fluid dynamics

associated with a polygon cylinder can be significantly different from that involving a circular or a square cylinder even under the same flow conditions, as will be demonstrated in this work.

Among the relatively limited number of research on the polygon cylinder wake, Tian & Li (2007) investigated a polygon cylinder of  $N = 24$  (N24 in abbreviation, so for other polygons hereafter) in a low speed wind tunnel to seek a low drag solution for their prototype supporting frames. They found a much lower critical Reynolds number ( $\approx 1.0 \times 10^5$ ) and 40% drag deduction with a low level fluctuation compared to a circular cylinder case under similar flow conditions. Bosch & Guterres (2001) tested a N8 tapered cylinder in their wind tunnel at  $Re \approx 3.0 \times 10^3 \sim 2.0 \times 10^4$  and found that the drag for the face orientation is lower than that for the corner orientation, and the degree of taper has a significant effect on the aerodynamic performance. Skews (1991, 1998) found that the polygon cylinder, whose ends were not fixed, with  $N < 8$  may undergo a spontaneous rotation, producing a larger lift than a circular cylinder at a similar rotation condition. Srigrarom & Koh (2008) conducted flow visualisation and phase-locked Particle Image Velocimetry (PIV) measurements on an equilateral triangular cylinder and found that, at certain uniform incoming flow velocities, the cylinder can oscillate persistently after an initial perturbation. Deniz & Staubli (1997) performed force and flow visualisation measurements for transversely oscillating rectangular and octagonal profiles and found that the mechanisms leading to an energy transfer from the fluid to the structures are associated with the phase shift of the fluctuating lift forces with respect to the body oscillation.

There have been attempts to simulate numerically the flow around a polygon cylinder. Tian & Wu (2009) calculated the flow field around the two-dimensional polygon cylinders at the corner orientation condition for even  $N$ s and  $Re < 200$ . They found through conformal mapping that, for the inviscid flow cases, the global pressure difference along the surface is inversely proportional to  $N$  that is sufficiently large. For the viscous flow cases, however, they derived the relation between the first critical  $Re$  and  $N$ , and found that this  $Re$  decreases as  $N$  increases. Khaledi & Andersson (2011) investigated numerically flow after a hexagonal cylinder for both corner- and face-oriented cases up to  $Re = 10^3$  and found that vortex shedding frequency is higher in the latter case, which is opposite to the earlier findings for the square cylinders (e.g. Vickery 1966). The numerical works mentioned are inevitably limited to  $Re$  lower than that typically seen in engineering applications.

To the best of the authors' knowledge, there has been no systematic experimental investigation on the wake of a polygon cylinder for  $N \geq 5$ , especially for pentagonal and septilateral cylinders. This work aims to address this issue by measuring  $C_D$ ,  $C'_L$  and  $St$  and determining their dependence on  $N$ , along with the major flow characteristics, for different polygon orientations (corner or face).

## 2. Experimental details

Experiments were conducted in an open-loop low-speed wind tunnel, which has a square test section of  $0.5\text{m} \times 0.5\text{m} \times 2\text{m}$ . The wind speed is  $2 \sim 40\text{m/s}$  in the test section, and the turbulence intensity  $\epsilon$  is no more than 0.5% for the range of speeds presently concerned. A schematic diagram of the side view of the section is shown in figure 1, where the coordinate system  $(x, y, z)$  is defined. The tested model is installed vertically along the  $z$ -axis. The lower end of the model is mounted with a three-component force measurement transducer Kistler 9317B, which is connected to a four-channel signal amplifier Kistler 5073A and a data collection A/D board NI6221. The upper end is pin-supported on a

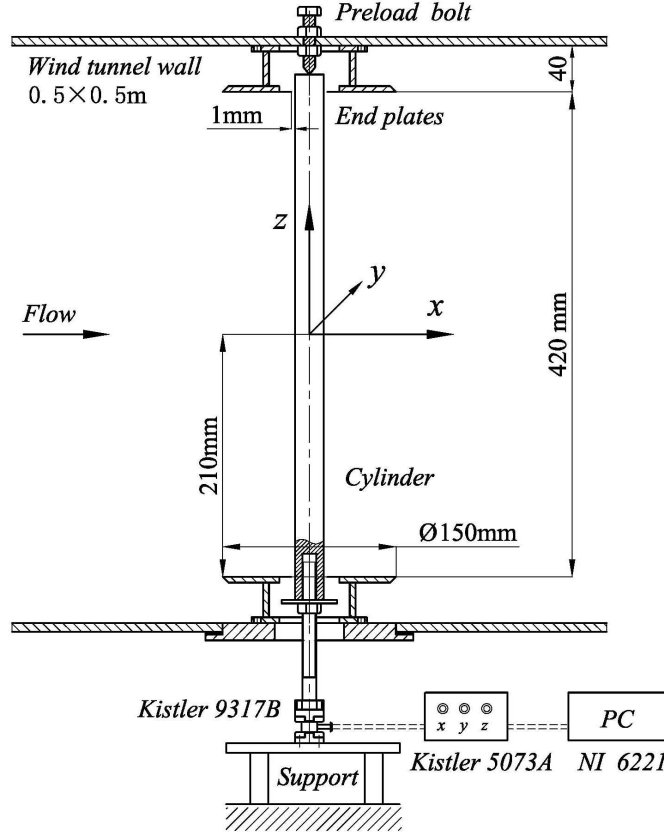


FIGURE 1. Schematic of the experimental set up.

pre-load bolt, which acts to eliminate the flow-induced cylinder vibration. Two circular-shaped end plates of  $\text{Ø}150\text{mm}$ , typically  $6 \times$  the longitudinally projected width  $D$  (see figure 2 for definition) of the test model, are attached near the two ends of the cylinder to eliminate the three-dimensional effects from the cylinder end and the possible influence from the wind tunnel walls. The gap between the end plates and the cylinder surface is  $1\text{mm}$ . The purpose of the end plate will be further elaborated at the end of this section.

The tested models include a flat plate ( $N = 2$ ), the polygon cylinders of  $N = 3 \sim 8$ , 12, 16, and a circular cylinder ( $N = \infty$ ). Two principal orientations with respect to the incoming flow are examined for each of the polygon cylinders, i.e. the face orientation, where one flat surface of the polygon faces normally to the incoming flow (denoted by NF), and the corner orientation, where the polygon is rotated so that one corner of it faces the incoming flow (denoted by NC), as shown in figure 2, where the orientation of the flat plate is also given. When placed in parallel with incoming flow, the flat plate is not considered as a bluff body and therefore is not tested. For most of the test cases,  $D = 25\text{mm}$ , resulting in a blockage ratio  $\phi \approx 5\%$ . Larger  $D$ , up to  $50\text{mm}$ , is also used for some cases to obtain the data of a larger  $\text{Re}$ , which will be discussed later. All the cylinders are made from aluminium with a length  $L = 460\text{mm}$  ( $420\text{mm}$  between the end plates) and an aspect ratio  $L/D = 16.8$  for  $D = 25\text{mm}$ .

Load cells Kistler 9317B and Kistler 5073A are used to measure the time-averaged drag coefficient  $C_D$  and the fluctuating (rms) lift coefficient  $C'_L$ . The resolution of the trans-

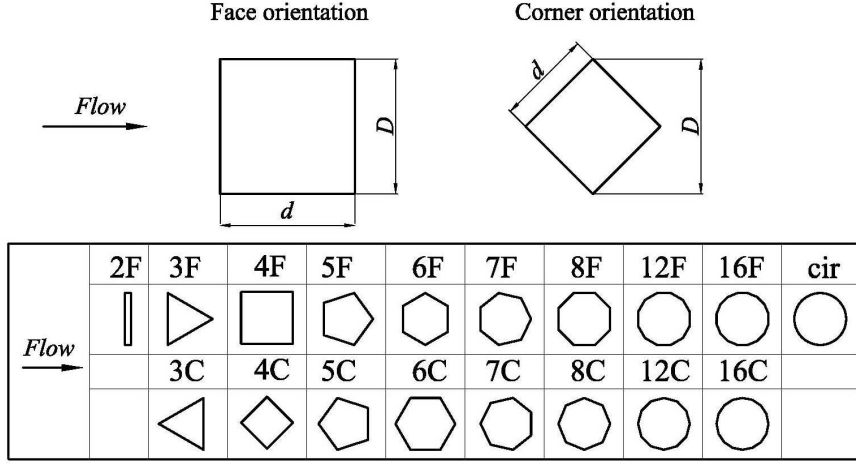


FIGURE 2. Cross-sectional shapes, orientations (with respect to the incoming flow) and notations of the 18 tested polygon cylinders ( $2 \leq N \leq 16$ ) and the definition of the streamwisely projected width  $D$ . In notation/abbreviation NF and NC,  $N$  is the polygon side number and F and C stand for orientations with a polygon flat surface and a corner, respectively, leading and facing normally to the incoming flow.

ducer is sufficiently high for our purpose (Alam & Zhou 2007). The force measurement signal is sampled at 5kHz, which is about 12 times the highest  $f_s$  from the cylinders. The sampling duration for each test is 5sec. The Strouhal number  $St = f_s D / U_\infty$  is also extracted from the force signal. The agreement of the measured cylinder oscillation frequency and  $f_s$  is confirmed by a simultaneous hot-film measurement at  $2.5D$  downstream of the cylinders at the mid-span location (figure not shown).

Figure 3 presents a comparison between the presently measured  $C_D$  and  $St$  for the circular cylinder and 4F cases and those reported in the literature. Evidently, for the examined  $Re$  range,  $C_D$  of the circular cylinder agrees well with Tropea *et al.* (2007), and so does that of 4F with White (2001). The maximum deviation is about 5%. Agreement in  $St$  is also quite good between the present and previously reported data; the departure is no more than 2% over the entire  $Re$  range examined.

The flow field is measured both qualitatively and quantitatively at a frame rate of 4 Hz by a LaVision PIV system, which consists of an Imager ProX camera with  $2048 \times 2048$  pixel CCD size and a low speed duo-head Nd:YAG laser. The field of view (FOV) of camera is typically  $125\text{mm} \times 125\text{mm}$ . Flow is seeded by smoke generated from vegetable oil with a droplet size around  $1\mu\text{m}$  in diameter. The smoke generator is located between six honeycomb meshes in the settling chamber of the wind tunnel, so that the smoke particles can be well mixed with air and form homogeneous smoke streaks. The PIV images are processed by DaVis 7.2 with final interrogation window (IW) size  $32\text{pixel} \times 32\text{pixel}$  and 50% overlap which gives a spatial resolution of  $1.95\text{mm}$  based on the IW size. For each test case, 100 velocity fields are acquired. Note that turbulence quantities are not of interest in this work. Smoke streak images are also used for flow visualisation after an appropriate increase of the laser power and the smoke particle density.

All experiments were conducted under room conditions. The  $Re$  range is  $1.0 \times 10^4 \sim 6.0 \times 10^4$ . All the data presented in this paper for  $Re \leq 6.0 \times 10^4$  are from the cylinders of  $D = 25\text{mm}$ . Cylinders of  $D = 50\text{mm}$  are used for some cases in order to extend the  $Re$  range to the order of  $10^5$ . The  $Re$  for the PIV measurements are fixed at  $1 \times 10^4$ . Each testing case is measured more than three times to ensure repeatability.

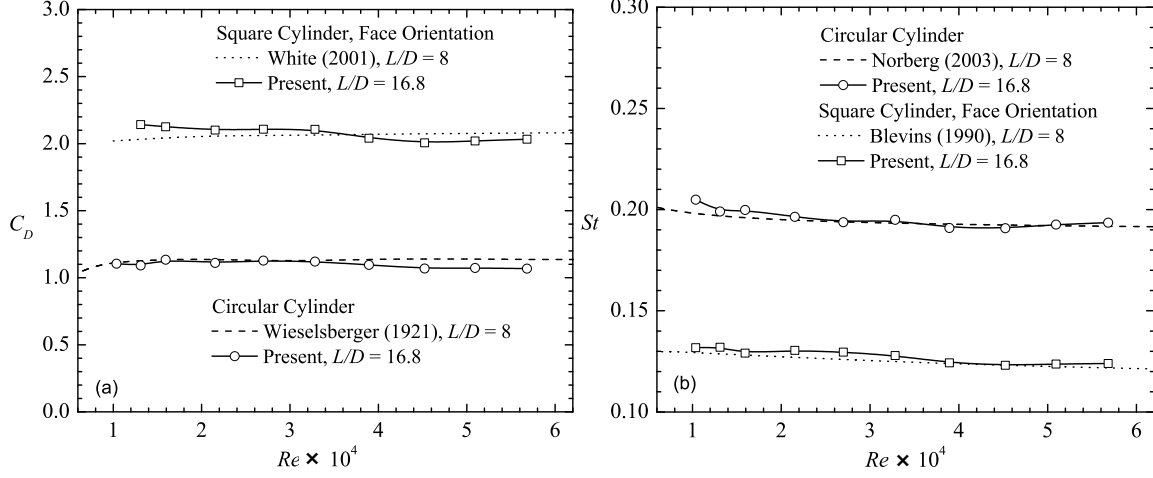


FIGURE 3. Dependence of  $C_D$  (a) and  $St$  (b) on  $Re$  for the case of 4F and the circular cylinder, as compared to the data available in the literatures. Results are obtained from an average of seven repeated measurements.

West & Apelt (1982) found that the effect of  $\phi$ , if less than 6%, is minor on  $C_D$  and negligible on  $St$ . They suggested that a correction is needed if  $\phi > 6\%$ . The correction factor is a function of  $\phi$  and  $C_D$  may decrease by 3% ~ 5% after applying the correction. No correction is applied presently since  $C_D$  and  $St$  obtained from larger  $D$  cylinders are found to be consistent with their counterparts from the cylinders of small  $D$ .

It is worth pointing out that it is impossible to eliminate completely the three-dimensional end effects on the flow even if the end plates are installed and  $L/D$  is kept large (Norberg 1994). Nevertheless, we have observed a considerable influence on the aerodynamic loading on the circular cylinder when the end plates are removed: the  $C_D$  drops by 20% and  $St$  by 10%, which is in agreement with previous reports by e.g. Cowdrey (1962), Gerich & Echelmann (1982) and Szepessy & Bearman (1992). Norberg (1994) also pointed out that for  $1.0 \times 10^4 < Re < 4.0 \times 10^4$ ,  $L/D$  should be no-less than 25 to ensure good two-dimensionality. However, the agreement of the present results to the previous ones shown in figure 3 indicates that the present  $L/D = 16.8$  is acceptable.

### 3. Results

#### 3.1. The effect of $Re$ on $C_D$ and $St$

The dependence of  $C_D$  and  $St$  on  $Re$  has been well documented for the polygon cylinders of  $N \leq 4$  and  $N = \infty$ . This work will be focused on the polygon cylinders of  $N > 4$ , for which the information on  $C_D$  and  $St$  is scarce in the literature. Table 1 lists the presently measured  $C_D$  and  $St$  at  $Re = 1.0 \times 10^4$ . The data for  $N \leq 4$  and  $N = \infty$  are also included for the purpose of comparison. There is in general a reasonable agreement between the present data and those in Tropea *et al.* (2007). There is a significant discrepancy in  $C_D$  and  $St$  for the case of 3C, marked by #. This is because the cross-sectional shape of the cylinder in Tropea *et al.* (2007) is a  $90^\circ$  wedge, different from the present equilateral triangle. The present  $St$  for 2F is lower than that in Tropea *et al.* (2007), marked by an asterisk, but is closer to that (0.13) reported in Blevins (1990).

Figure 4 shows how  $C_D$  and  $St$  change as  $Re$  varies from  $1.0 \times 10^4$  to  $5.8 \times 10^4$ , for all polygon cylinders at both principal orientations, including the flat plate (2F) and



Case	Present Re = $1.0 \times 10^4$		Tropea <i>et al.</i> (2007) Re $\approx 10^4$	
	$C_D$	St	$C_D$	St
2F	2.250	0.143	2.0	0.16*
3C	1.179	0.200	1.6 <sup>#</sup>	0.18 <sup>#</sup>
3F	2.086	0.127	2.0 <sup>#</sup>	0.14 <sup>#</sup>
4C	1.628	0.167	1.6	0.15
4F	2.100	0.132	2.1	0.13
5C	1.627	0.140	/	/
5F	1.146	0.202	/	/
6C	1.866	0.138	/	/
6F	1.375	0.178	/	/
7C	1.228	0.169	/	/
7F	1.663	0.155	/	/
8C	0.950	0.195	/	/
8F	1.566	0.148	/	/
12C	1.220	0.183	/	/
12F	1.366	0.174	/	/
16C	1.050	0.185	/	/
16F	1.292	0.186	/	/
Cir	1.105	0.205	1.2	0.21

TABLE 1. The present  $C_D$  and St values obtained at Re =  $1.0 \times 10^4$ . Also included are the reported data in Tropea *et al.* (2007).

the circular cylinder. The  $C_D$  of the N12 and N16 cylinders declines rather rapidly from Re  $\approx 3.0 \times 10^4$  to  $4.0 \times 10^4$  and meanwhile the corresponding St rises sharply. The observation points to a boundary transition from laminar to turbulent state. The effect of the transition on the changes of  $C_D$  and St can differ significantly when the cylinder changes its orientation. For example,  $C_D$  decreases by 25% and St increases by 15% from Re  $\approx 2.4 \times 10^4$  to  $3.0 \times 10^4$  for the 12C orientation, but the changes contract to 15% and 5%, respectively, for the 12F orientation. Furthermore, the Re at which the transition starts to take place also varies from one orientation to the other. It can be inferred that the flow characteristics can be very different between the two orientations. On the other hand,  $C_D$  and St for  $N \leq 8$  cylinders vary little, within  $\pm 8\%$  and  $\pm 4\%$ , respectively, over the entire Re range, suggesting no change of the boundary layer state.

Figure 5 (a) summarises the variation in the critical Reynolds number Re<sub>c</sub>, at which the boundary layer transition from laminar to turbulent state occurs, with increasing N for the NC cases. The N24 case from Tian & Li (2007) and the circular cylinder case (N = ∞) from White (2001) are also included. The Re<sub>c</sub> is defined at the middle of the rapidly falling  $C_D$  region in figure 4 (a). The  $C_D$  values before and after the transition, i.e.  $C_{D-sub}$  and  $C_{D-sup}$ , are also presented for each case. The NF cases are not shown since the transition effect on 12F is not very strong. Clearly, both Re<sub>c</sub> and  $\Delta C_D = (C_{D-sub} - C_{D-sup})$  rise with increasing N. The dependence of Re<sub>c</sub> on N may be used to estimate Re<sub>c</sub> for the polygons that are not measured presently. For instance, the Re<sub>c</sub> of the 20C case is predicted to be about  $7.0 \times 10^4$ .

Given an adequately large N, the corners of a polygon cylinder may be considered to be wedge-shaped roughness elements evenly distributed on the surface of a circular cylinder with a radius  $R_i$ . Denoting the distance between one corner and the polygon



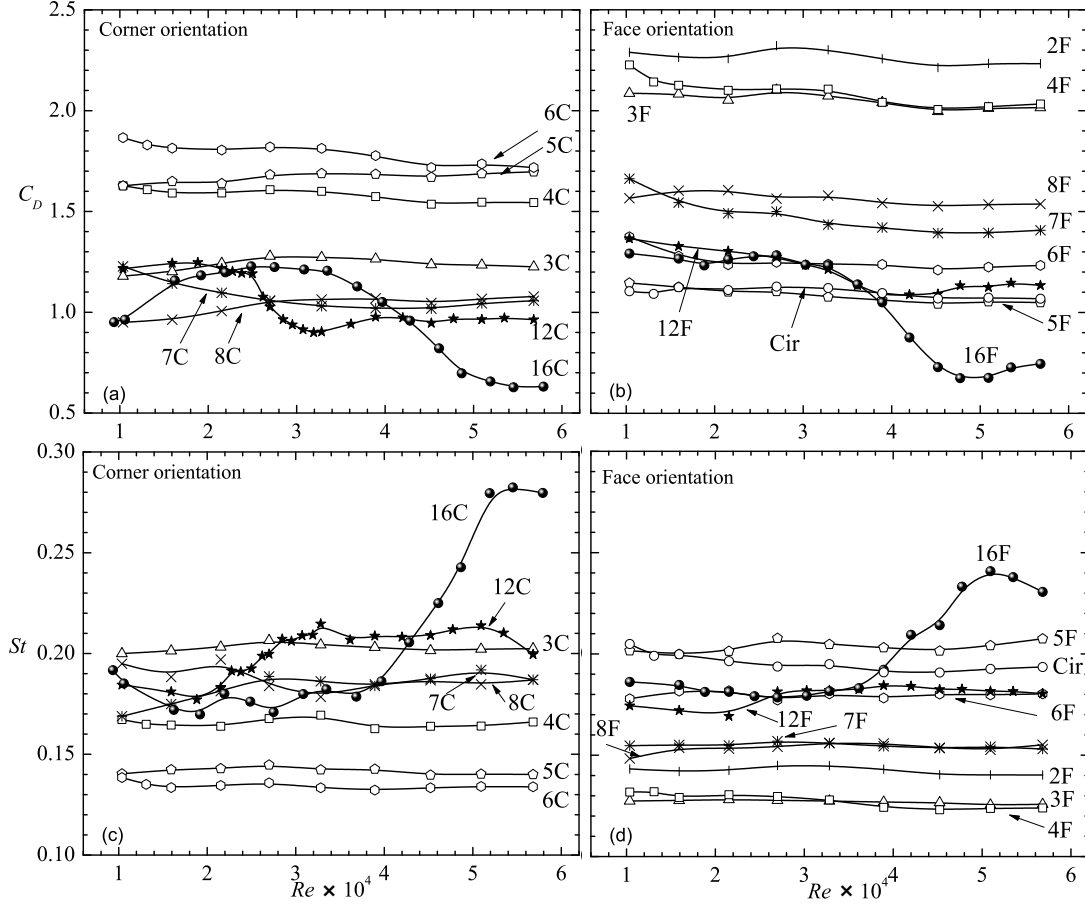


FIGURE 4. Dependence of  $C_D$  and  $St$  on  $Re$  for both principal orientations. (a)  $C_D$  for NC; (b)  $C_D$  for NF; (c)  $St$  for NC; (d)  $St$  for NF; the cases for the flat plate and the circular cylinder are also included, denoted as 2F and Cir, respectively, in (b) and (d).

centroid as  $R_o$ , the roughness height  $\varepsilon$  can be written as:

$$\frac{\varepsilon}{D} = \frac{R_o - R_i}{D} \approx \frac{1 - \cos(\pi/N)}{2}. \quad (3.1)$$

In an attempt to understand the positive correlation between  $Re_c$  and  $N$  shown in figure 5 (a),  $Re_c$  is plotted against  $\varepsilon/D$  in (b). One may recognise that the variation in  $Re_c$  against  $\varepsilon/D$  for large  $N$  polygon cylinders agrees reasonably well both qualitatively and quantitatively with its counterpart for the rough-surfaced circular cylinders. It may be inferred that, given an adequately large  $N$ ,  $Re_c$  of the polygon cylinder may be estimated from that of the rough-surfaced circular cylinder, subjected to a small uncertainty. Güven *et al.* (1980) observed that larger roughness elements on the surface of a circular cylinder gave rise to a thicker and more retarded boundary layer. As a result, the transition to turbulence occurred at lower  $Re$ . As the roughness elements diminished in size, the drop in  $C_D$  from subcritical to supercritical regime became more pronounced. The result shown in figure 5, i.e. increasing  $Re_c$  and  $\Delta C_D$  with larger  $N$  or smaller  $\varepsilon/D$ , is fully consistent with their observation. The result further points to an analogy between polygon cylinders of large  $N$  and roughened circular cylinders.

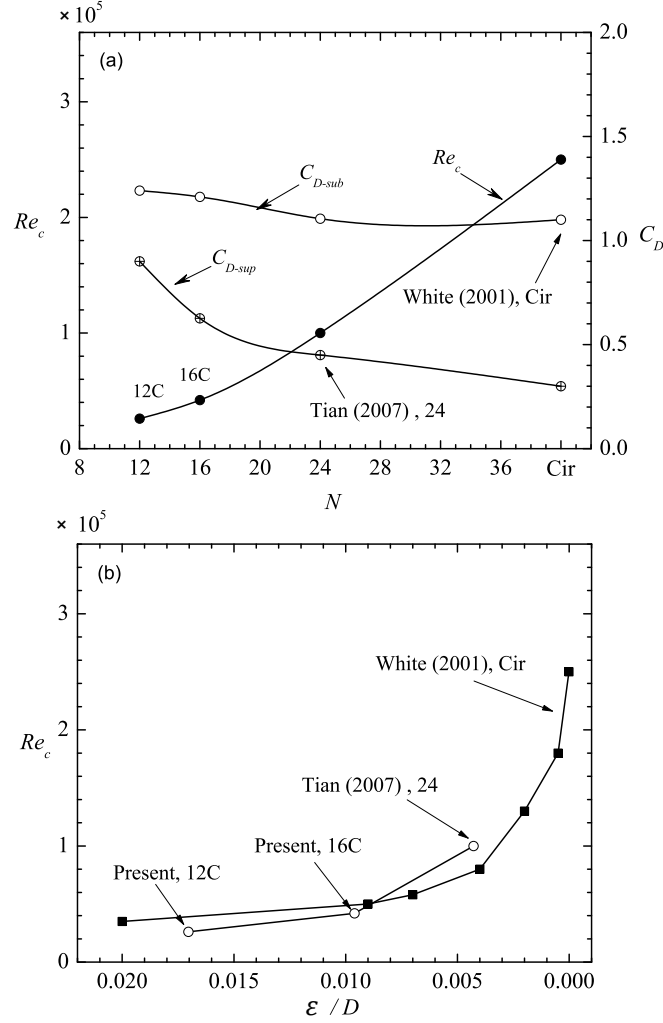


FIGURE 5. (a) Dependence of the critical Reynolds number  $Re_c$  ( $\bullet$ ),  $C_{D-sub}$  ( $\circ$ ) and  $C_{D-sup}$  on the polygon side number  $N$ , for  $N \geq 12$  for the corner orientation. (b) Dependence of  $Re_c$  on the roughness height  $\varepsilon/D$ ;  $\circ$ : polygons,  $\blacksquare$ : circular cylinders with roughness elements.

Note that figure 5 (b) includes only the cases of  $N \geq 12$ . For  $N \leq 8$ , the corner number of the polygon is so few that  $(R_o - R_i)$  becomes relatively large compared to the characteristic dimension  $R_i$  of the polygon and cannot be approximated as roughness elements any more. Therefore, the analogy between the polygon corners and roughness elements is no longer valid.

### 3.2. Dependence on $N$ of $C_D$ , $St$ and $C'_L$

Figure 6 presents the dependence on  $N$  of the measured  $C_D$  and  $St$  for both orientations of the polygons at  $Re = 2.0 \times 10^4$  and  $5.0 \times 10^4$ , which correspond to the flow before and after the transition, respectively, of the N12 and N16 polygons. One may note that at small  $N$  the  $C_D$  or  $St$  values differ greatly between the two orientations. However, this difference diminishes as  $N$  becomes large, regardless of the orientation. While  $C_D$  in general tends to decline with increasing  $N$ ,  $St$  rises. There is another interesting observation, that is, the

NF and NC data points ( $C_D$  and  $St$ ) appear forming a distorted Cartesian mesh pattern, as highlighted by the solid and dashed lines. It is worthwhile conducting an analysis of the mesh pattern, which can be of practical importance, i.e. predicting  $C_D$  and  $St$  for the polygon cylinders not measured presently. Four solid lines can be identified for each  $Re$ , viz.

- (a)  $I_1$ ,  $N = 2n + 1$ ;  $C$  oriented for odd  $n$ ;  $F$  oriented for even  $n$
- (b)  $II_1$ ,  $N = 2n$ ;  $C$  oriented for even  $n$ ;  $F$  oriented for odd  $n$
- (c)  $I_2$ ,  $N = 2n + 1$ ;  $F$  oriented for odd  $n$ ;  $C$  oriented for even  $n$
- (d)  $II_2$ ,  $N = 2n$ ;  $F$  oriented for even  $n$ ;  $C$  oriented for odd  $n$

On each of the four solid lines, the  $F$ - and  $C$ -orientated data points are separated by each other, provided that the untested cases (e.g.  $N = 9, 10$ ), which can be estimated from the available data, are also included. The estimation of the untested cases will be explained below. There are actually more dashed lines than those marked in figure 6. For example,  $2F-3F-4F$  can also form one. Unlike the solid lines, the data points along each of the dashed lines are either uniformly  $F$  or uniformly  $C$  orientation. This particular pattern is essentially connected to the geometry of the polygons near the lateral maximum width points (the top and the bottom point) and the position of the flow separation point if the transition takes place ( $N = 12, 16$ ), which will be discussed in § 3.4.

The pattern shown in figure 6 can be used to predict approximately  $C_D$  and  $St$  for the cases that are not tested in the current experiment. For instance, based on the characteristics of the solid lines listed from item (a) to item (d) above, it can be predicted from figure 6 (b) that case  $10C$  should be on the solid line  $II_2$  and can be determined at the intersection of  $II_2$  and  $N = 10$ . Connecting points  $7C$ ,  $8C$  and  $10C$  smoothly forms a new dashed line as shown in figure 6 (b), which displays a similar trend to the other two dashed lines. The intersection of this newly constructed dashed line and  $N = 9$  gives the position of  $9C$ . Obviously, curve  $II_2$ , if extrapolated, passes almost precisely point  $9C$ . As a result,  $C_D$  of  $9C$  at  $Re = 5.0 \times 10^4$  is estimated to be 1.25 and  $C_D$  of  $10C$  to be 1.40, with a caveat of a small uncertainty. Following the same procedure, we may also estimate from figure 6(d) that  $St$  of  $9C \approx 0.170$  and  $St$  of  $10C \approx 0.165$  at  $Re = 5.0 \times 10^4$ .

It is more difficult to predict  $C_D$  and  $St$  for polygons of  $N \geq 16$ , which requires an extrapolation of the known data. However, it is possible to predict a general trend of  $C_D$  and  $St$  for the tested  $Re$  range. Recall that circular cylinders can be treated as  $N = \infty$ . Figure 5 can be used to estimate the  $Re_c$  of large  $N$  polygons. Given  $N = 18$ ,  $Re_c$  is found to be approximately  $5.0 \times 10^4$  and a larger  $N$  indicates an even higher  $Re_c$ . We may thus deduce that the flow at  $Re = 2.0 \times 10^4$  (figure 6 a and c) is in the subcritical regime, implying that the two points between  $N = 16$  and  $\infty$  can be connected smoothly, as shown in figure 6 (a) and (c).

At  $Re = 5.0 \times 10^4$  (figure 6 b and d), however, the variation in  $C_D$  and  $St$  is more complicated once the transition has taken place for the polygon of large  $N$ , say  $N = 18$ . There are two turning points in each  $C_D$  and  $St$  line, as marked by  $+$  symbols in figure 6 (b) and (d). As  $Re_c$  is defined at the middle of a transitional  $Re$  range, typically over  $Re_c - 1.0 \times 10^4 \sim Re_c + 1.0 \times 10^4$ . As such, the transition is likely to start at  $Re \approx 4.0 \times 10^4$  for  $N = 18$  polygon. Thus  $C_D$  and  $St$  for  $N = 18$  polygon should follow the trend of  $N12$  and  $N16$  polygons where the transition occurs, as indicated by the symbol  $+$  at  $N = 18$  in figure 6 (b) and (d). Note that  $Re_c$  is even higher for  $N > 18$ . For example, as estimated in figure 5,  $Re_c \approx 6.0 \times 10^4$  for  $N = 19$ . Therefore, at  $Re = 5.0 \times 10^4$ , the  $N19$  cylinder is less likely to be in the transition, which implies that  $St$  would drop and  $C_D$  would increase markedly, compared to their counterparts at  $N = 18$ . Moreover, as  $N$  increases,  $C_D$  and  $St$  will asymptotically approach their counterparts of the circular cylinder and their values will vary little because the subcritical flow condition remains unchanged

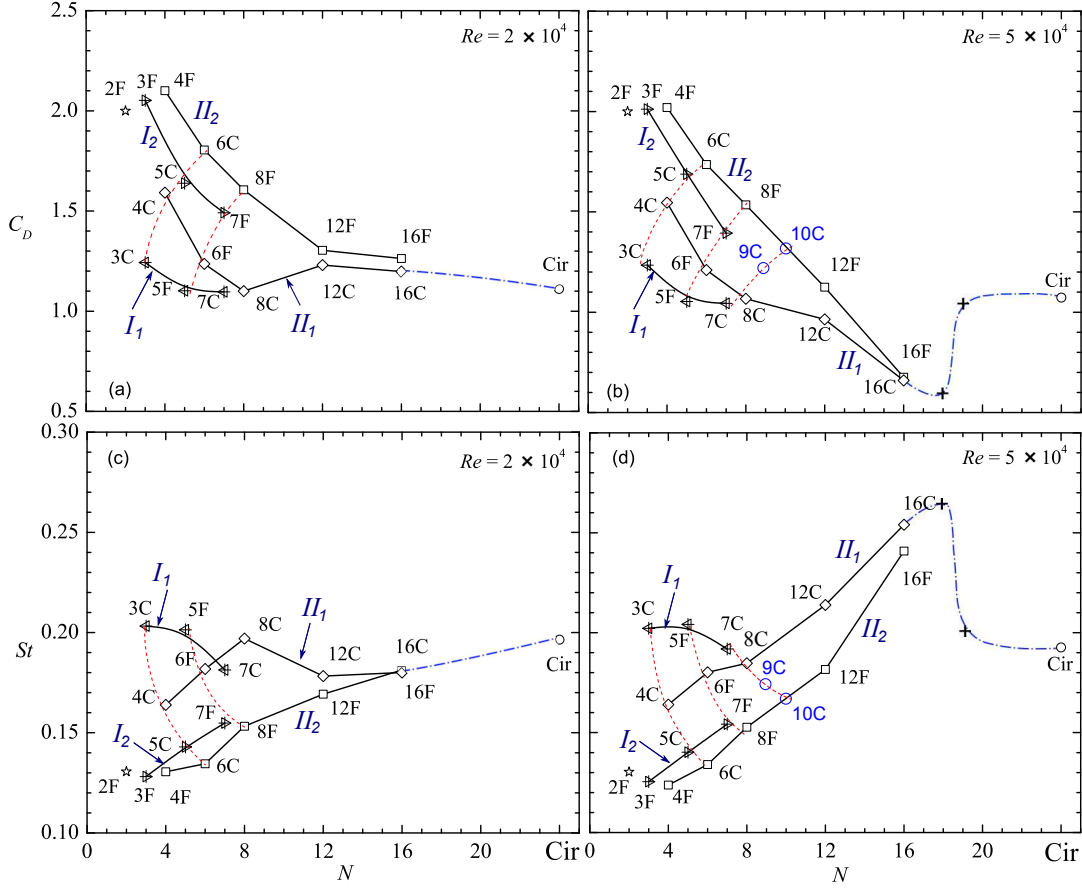


FIGURE 6. Dependence of  $C_D$  (a-b) and  $St$  (c-d) on the polygon side number  $N$  for  $Re < Re_c$  (a, c) and  $Re > Re_c$  (b, d). The transition occurs at  $N = 12, 16$ . Data points 9C and 10C in (b) are two examples of the predicted results. The dash-dot lines denote the indicative trend for the polygons of large  $N$ . The data points of 2F in (a) and (b) are from Tropea *et al.* (2007) and from Blevins (1990) in (c) and (d). The two + symbols in each (b) and (d) indicate the turning points of the indicative trend lines from  $N = 16$  to the circular cylinder.

when  $N \rightarrow \infty$ . Therefore, another turning point + at  $N = 19$  is predicted, which is connected smoothly to the value of  $N = \infty$  in figure 6 (b) and (d).

Figure 7 presents the dependence of the fluctuating lift coefficient  $C'_L$  on  $N$ . In order to avoid the influence of the synchronisation between vortex shedding and the natural frequency of the cylinder, the  $C'_L$  measurement is limited to  $U_\infty$  at which  $f_s < 80\text{Hz}$ . The data at  $Re = 1.6 \times 10^4$  are illustrated. A number of observations can be made. Firstly, the present  $C'_L$  on the circular cylinder agrees very well with Norberg (2003), which provides a validation for our measurements. Secondly, for either orientation,  $C'_L$  rises rapidly first with increasing  $N$ , reaching the maximum at 4F and 6C, respectively, and then drops quickly before approaching the value of  $N = \infty$ . Finally,  $C'_L$  varies greatly from one orientation to the other for  $N < 7$  but becomes identical to each other for  $N \geq 12$ , implying that  $C'_L$  becomes independent of the cylinder orientation for large  $N$ . The result is consistent with the proposed analogy between the polygon cylinder of  $N \geq 12$  and the roughened circular cylinder.

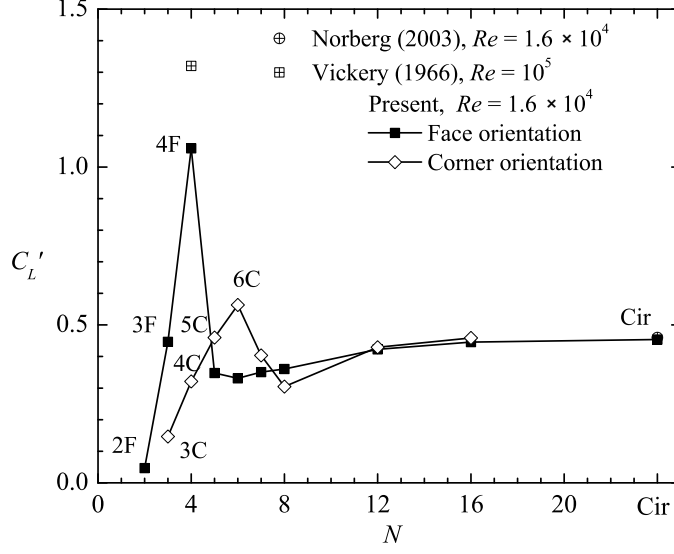


FIGURE 7. Dependence of the lift coefficient  $C'_L$  on  $N$ . Note that the data of the circular cylinder from Norberg (2003) is also included, which collapses almost completely with the present measurement.

### 3.3. Wake characteristics

In this section, a number of wake characteristic length scales are extracted from the time-averaged velocity fields obtained from the PIV data. The length scales are further used to define the wake Strouhal number and the wake drag coefficient.

Figure 8 uses the 5C case to illustrate the definitions of wake length scales, where asterisks denote normalisations by  $D$  and/or  $U_\infty$ . One important quantity is the flow separation angle  $\theta_s$ , which is defined as the angle between  $U_\infty$  and  $\overline{U}_{sp}^*$ , where  $\overline{U}_{sp}^*$  is the tangential velocity at the separation point along the separation streamline. For the 5C case, the two angles  $\theta_o$  (the separation point location) and  $\theta_s$  are related by:

$$\theta_s = \pi - (\theta_o + \varphi/2) = \pi/2 + \pi/N - \theta_o, \quad (3.2)$$

where  $\varphi = (N-2)\pi/N$ . The general relation of  $\theta_s$  to the geometry and the orientation is not so straightforward. Note that the separation angle is defined differently from Tropea *et al.* (2007), where  $\theta_o$  is defined as the separation angle. The reason for this different definition and a more detailed discussion of  $\theta_s$  will be given in § 3.4. The marked streamlines pass through the separation points, which are also the free streamlines closest to the centreline. The reversed flow zone, defined by  $\overline{U}_x^* = 0$ , is marked by the streamline passing through the wake stagnation point located at  $x_R^*$  downstream of the polygon centroid  $O$ . The maximum wake width  $D_w^*$  is measured at  $x_w^*$  downstream of  $O$ .  $\overline{U}_w^*$  is the tangential velocity at the maximum wake width point  $(x_w^*, y_w^*)$  along the streamline through the separation point.

Figure 9 presents the dependences of  $x_R^*$ ,  $D_w^*$ ,  $x_w^*$  on  $N$ , which are quite similar to each other. Not surprisingly,  $x_R^* \approx 2x_w^*$ . Different orientations result in a difference in  $x_R^*$ ,  $D_w^*$  or  $x_w^*$ , especially for  $4 \leq N \leq 8$ . Even though the blockage ratios are the same for all the cylinders, a different degree in bluntness may also have an impact on the back pressure, the separation shear layers and hence the structure of the wake (Roshko 1955). For  $N \geq 12$ ,  $D_w^*$  remains roughly constant and is almost the same as that in the circular

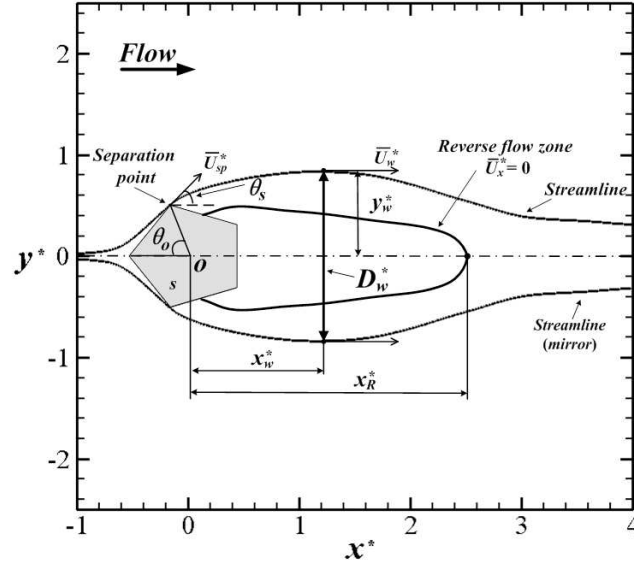


FIGURE 8. Definitions of various characteristic length and velocity scales in the dimensionless form for polygon cylinder wake. Asterisks denote normalisations by  $D$  and/or  $U_\infty$ . Note that the free streamlines and reversed flow zone are drawn based on the PIV data obtained at  $Re = 1.0 \times 10^4$ . The bottom streamline uses the mirror image of the top one due to the shadow of the cylinder (laser illumination comes from above).

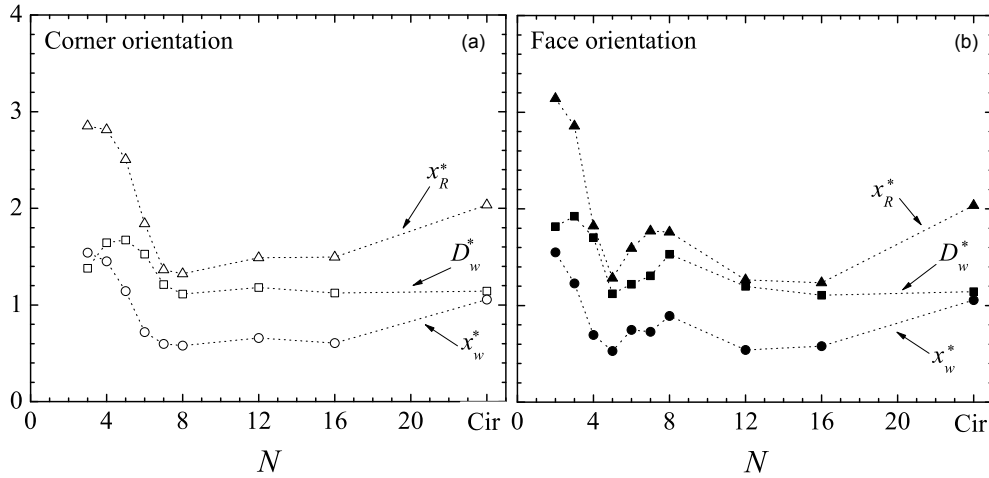


FIGURE 9. The dimensionless characteristic length scales ( $x_R^*$ ,  $D_w^*$ ,  $x_w^*$ , defined in figure 8) as functions of  $N$ , at  $Re = 1.0 \times 10^4$ .

cylinder wake, but the streamwise length scales  $x_R^*$  and  $x_w^*$  are both significantly smaller. Note that  $Re$  in figure 9 is well below  $Re_c$ .

Based on the momentum equation, the drag on a bluff body can be calculated from its wake parameters (length and velocity scales) and independently on the geometry of the bluff body itself (Antonia & Rajagopalan 1990). Roshko (1955) proposed that there exists a universal similarity for the vortex shedding patterns and the wake structures among differently shaped bluff bodies. Once  $(C_p)_b$  is determined,  $St^R$  in equation 1.1 is

found to be

$$\text{St}^R = \left(1 - \frac{u}{U_\infty}\right) \left(\frac{D_w}{l}\right) \left(\frac{1}{\sqrt{1 - (C_p)_b}}\right) \approx 0.15 \sim 0.17, \quad (3.3)$$

where  $l$  is the longitudinal vortex spacing, and  $u$  is the convection velocity of the vortices. Williamson & Brown (1998) proposed a corrected universal Strouhal number  $\text{St}^W$ , viz.

$$\text{St}^W = \left(\frac{f_s D}{U_\infty}\right) \frac{U_\infty}{U_s} \left(1 + \frac{2\delta}{D}\right) \approx 0.176, \quad (3.4)$$

where  $\delta$  is the characteristic shear layer thickness. Ahlborn *et al.* (2002) suggested another correction:

$$\text{St}^A = \beta \text{St} = \left(\frac{D_v}{D}\right) \text{St}, \quad (3.5)$$

where  $D_v$  is the equivalent diameter of the shed vortices. The resultant universal Strouhal number from different corrections vary quite significantly, which is partly due to the ways of determining  $D_w$  and  $U_s$ .

The use of the above mentioned universal Strouhal number reduces and sometimes eliminates the direct influence of the bluff body geometries, though inevitably involving more quantities to be measured with more uncertainties and measurement error. For simplicity, we replace only the length scale by  $D_w^*$  and define alternative  $C_D^+$  and  $\text{St}^+$ , i.e.

$$C_D^+ = C_D / D_w^*, \quad (3.6)$$

$$\text{St}^+ = \text{St} D_w^* = \frac{f_s D_w}{U_\infty}, \quad (3.7)$$

The dependences of  $C_D^+$  and  $\text{St}^+$  on  $N$  are presented in figure 10, along with those of  $C_D$  and  $\text{St}$ . The distorted Cartesian pattern observed in figure 6 disappears for both  $C_D^+$  and  $\text{St}^+$ ; rather, the data points are much less scattered. The  $C_D^+$  data occur about 1.0 and  $\text{St}^+$  near  $0.21 \sim 0.23$ , except for  $N \leq 4$ . It seems plausible that using the wake scales does have potential in getting the data collapsed and in establishing a possible correlation between  $C_D^+$  and  $\text{St}^+$  (a correlation, if any, seems to be rather weak from figure 10). Nevertheless, some data points still display a relatively large scatter, especially at small  $N$ . Note that involving the wake characteristics implies additional measurements to be conducted. It would be desirable to establish a direct correlation between  $C_D$  and  $\text{St}$ . We will propose a new scaling factor in § 3.5, which proves to work well for polygon cylinders.

### 3.4. Flow separation angle

In the context of a polygon cylinder, the flow separation angle  $\theta_s$  is in fact the angle between the particular polygon side upstream of the separation point and the incoming flow direction, that is, this angle may be directly determined from the separation point  $\theta_o$ , if known. The location of  $\theta_o$  and hence  $\theta_s$  can be fairly accurately found out by carefully examining the flow visualisation images, as illustrated in figure 11. The separation point of the polygon cylinders including the 2F case all occurs at one of the corners (above the wake centerline), except perhaps very large  $N$  such as the circular cylinder. The determined  $\theta_o$  and  $\theta_s$  at  $\text{Re} = 1.0 \times 10^4$  are indicated schematically in figure 12. The  $\theta_s$  for the circular cylinder is the angle between the incoming flow direction and the tangent line at the separation point. Note that, in cases of 5F and also 8C, flow separates first at



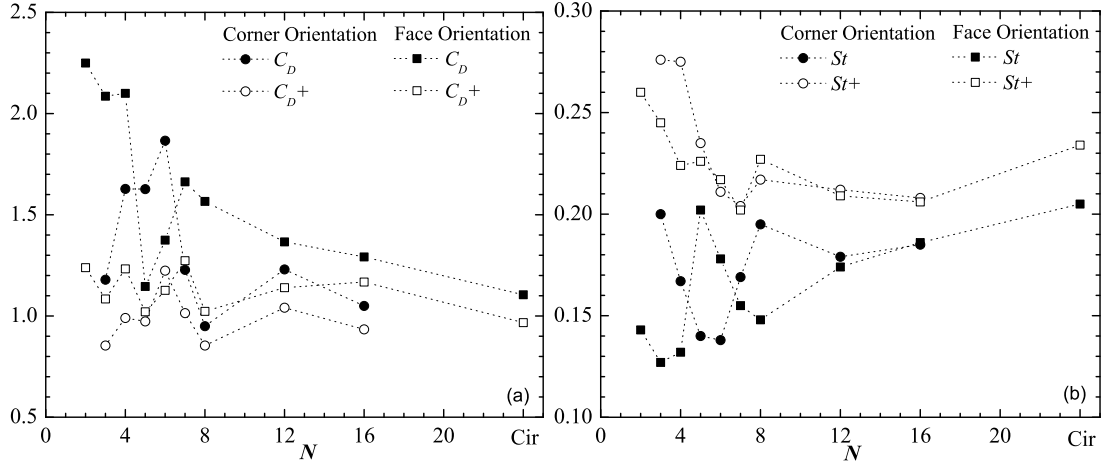


FIGURE 10. Dependence of the universal  $C_D^+$  and  $St^+$ , as compared to  $C_D$  and  $St$ , on  $N$ .  
 $Re = 1.0 \times 10^4$ .

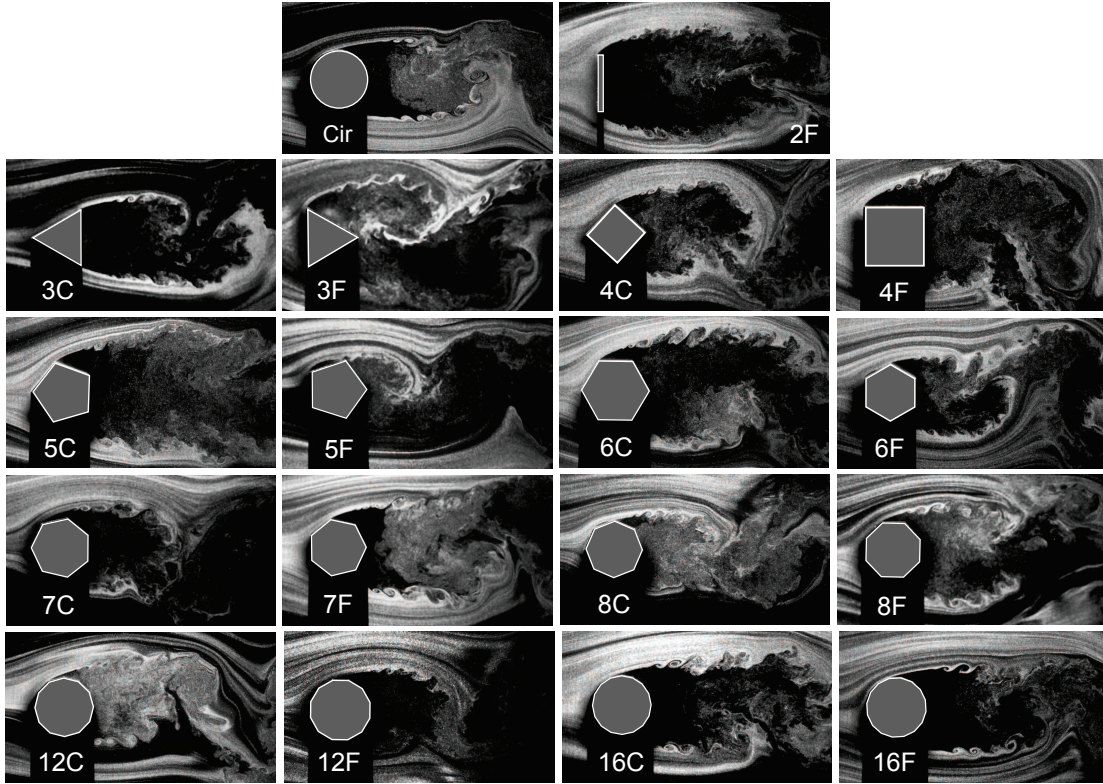


FIGURE 11. Smoke streak flow visualisation images for all the testing cases at  $Re = 1.0 \times 10^4$ .

corner A before reattaching to the polygon surface edge AB, and then separates again at B. Therefore, corner B is taken as the separation point.

It has been well established that  $C_D$  of the circular cylinder depends on the position of the separation point. For  $Re < Re_c$ , the laminar boundary layer separates fairly early,

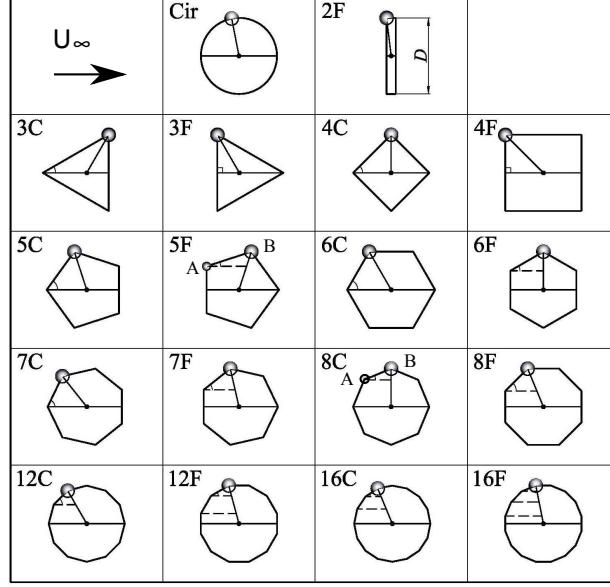


FIGURE 12. Schematic diagrams indicating the location of the separation point above the centreline, marked by a circle, and the separation angle  $\theta_s$ , marked by  $\angle$ , as determined at  $Re = 1.0 \times 10^4$ .

at  $\theta_o \approx 79^\circ$  and  $\theta_s \approx 11^\circ$ . For  $Re > Re_c$ , the transition occurs in the boundary layers and the flow separation is postponed, resulting in a lower  $C_D$ .

For the polygons of  $N \leq 4$ ,  $\theta_o$  is fixed and independent of  $Re$ .  $C_D$  changes little with  $Re$ .

For the polygons of  $5 \leq N \leq 8$ ,  $\theta_o$  is also fixed. To facilitate discussions, denote the point at the maximum lateral width as  $T_o$  and take the front one if two corners correspond to the maximum width position, as is the case for 6C, 8F, 12F and 16F (figure 12). Use  $T_1$  and WSP to represent the corner upstream of  $T_o$  and the windward stagnation point on the centerline, respectively. Four scenarios have been observed:

- (a) Flow separates at  $T_o$  and there is no corner between  $T_o$  and WSP, as the cases for 5C, 6C and  $N \leq 4$ , which are associated with the dashed line 3C-5C in figure 6;
- (b) Flow separates at  $T_o$  and there is one corner between  $T_o$  and WSP (6F, 7F, 8F);
- (c) Flow separates at  $T_1$  and the boundary layer reattaches and separates again right before  $T_o$  (5F, 8C);
- (d) Flow separates at  $T_1$  but does not reattach (7C).

For  $N \geq 12$ , the wake pattern is similar to that behind the circular cylinder, where the transition may have a pronounced effect on the flow. Nevertheless at  $Re < Re_c$ , the separation point is fixed at one corner. A few examples of flow around the polygon cylinders of  $N \geq 12$  at  $Re = 5.0 \times 10^4$  when the transition occurs (refer to figure 4) are shown in figure 13.

The dependence of  $\theta_s$  on  $N$  shows again a distorted Cartesian mesh pattern (not shown) similar to figure 6, which suggests a relation between  $C_D$  and  $\theta_s$ . As a matter of fact,  $\theta_s$  and  $C_D$  fall approximately on a linear correlation for most of the cases, as shown in figure 14. There are only a few cases that deviate from this linear correlation. It is found that the separation point occurs at  $T_o$  (see figures 11 and 12) for all the cases reasonably following the linear correlation. For 7F and 8C cases,  $T_o$  is actually the separation point of the reattached flow which initially separated at  $T_1$ . For these two cases, the flow is

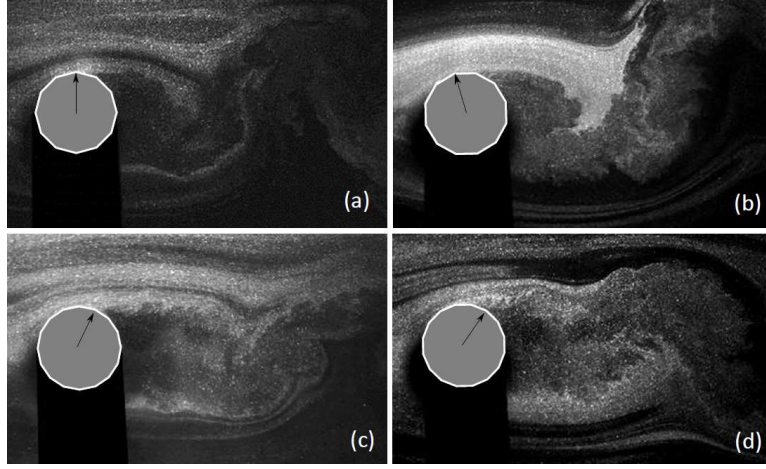


FIGURE 13. Smoke streak flow visualisation for (a) 12C, (b) 12F, (c) 16C and (d) 16F when the transition occurs.  $Re = 5.0 \times 10^4$ . The arrows indicate the approximate mean separation point, since instantaneously the separation point oscillates from one instant to the next.

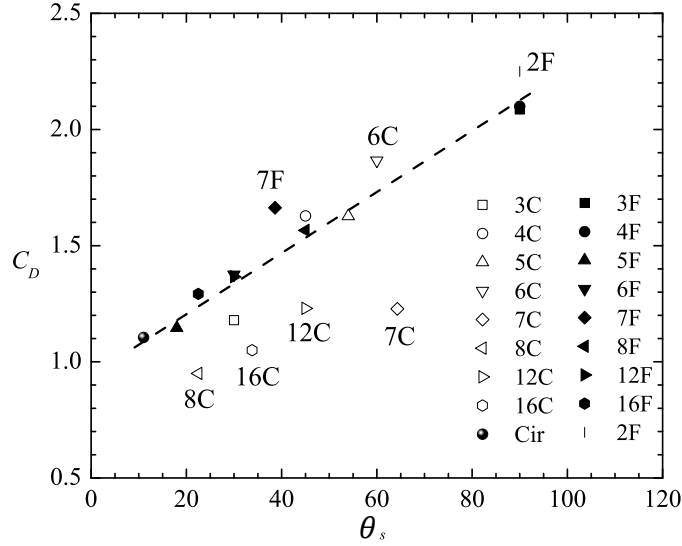


FIGURE 14. Correlation between  $C_D$  and  $\theta_s$  at  $Re = 1.0 \times 10^4$ .

more sensitive to  $Re$  and the data  $(\theta_s, C_D)$  deviate from the linear relation in figure 14. The other three data points which deviate further correspond to the cases 7C, 12C and 16C, when the flow separates at  $T_1$  without reattachment. In the cases showing large deviation to the linear relation, the lateral distance between the two separation points (above and below the centreline) is not the same as the characteristic length scale  $D$ .

In order to account for such deviations, we propose to define a new angle  $\xi$  associated with the point  $T_o$ , between two directions:

- (a) the direction from  $T_1$  to  $T_o$  and the incoming flow direction in the absence of the transition;
- (b) the direction from  $T_o$  to TP (the point where the transition occurs) and the incoming flow direction when the transition occurs (if TP is downstream of  $T_o$ ,  $\xi$  is negative);

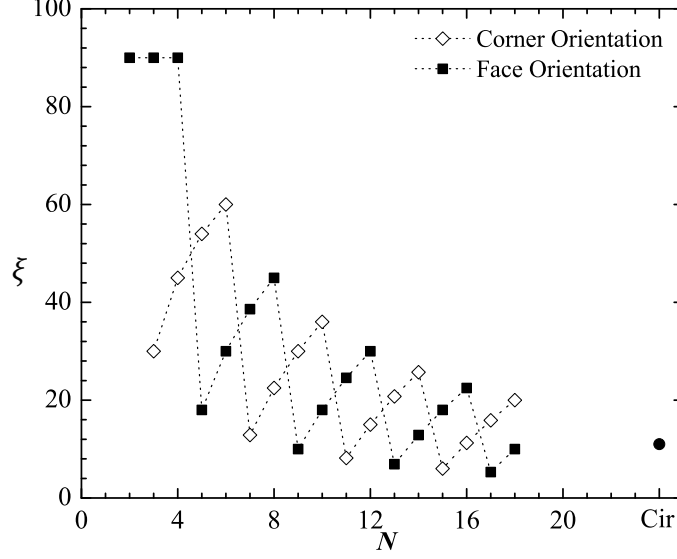


FIGURE 15. Dependence of the angle  $\xi$  on  $N$ , based on equation 3.8, in the absence of the transition.

(c) the tangent line at the separation point and the incoming flow direction for the circular cylinder case.

Thus defined  $\xi$  is underpinned by two observations: (1) in the absence of the transition,  $C_D$  depends only on  $N$  and the orientation, not on  $Re$ ; (2)  $T_o$  essentially defines the entire wind-ward surface, which effectively describes the degree of bluffness for a regular polygon of any  $N$ . In the absence of the transition,  $\xi$  can be mathematically written, in unit of degree, as:

$$\xi = \frac{180}{\pi} \times \begin{cases} \frac{\pi}{2} - \left(p - \frac{1}{2}\right) \left(\frac{2\pi}{N}\right), p = \left\lceil \frac{N-2}{4} \right\rceil, & NC \text{ cases;} \\ \frac{\pi}{2} - (q-1) \left(\frac{2\pi}{N}\right), q = \left\lceil \frac{N}{4} \right\rceil, & NF \text{ cases,} \end{cases} \quad (3.8)$$

where  $\lceil \cdot \rceil$  denotes the nearest larger integer. Note that  $\xi$  is calculated based on  $T_o$  above the centreline, which is not always the separation point. Therefore,  $\xi$  is sometimes different from  $\theta_s$ . Figure 15 presents the results calculated from equation 3.8, which displays a distorted Cartesian pattern similar to that in figure 6 (a); see the dashed lines. When  $Re \geq Re_c$ , for  $N = 12$  and  $N = 16$  cases,  $\xi$  depends also on  $Re$  and no analytical solution can be obtained simply on the geometry and orientation. The true value of  $\xi$  when the transition occurs can be measured from experiments. It is worth mentioning that beyond  $Re_c$ , the separation point is no longer fixed at a particular point; rather it oscillates around a mean location, which is determined from the average of the 100 smoke streak images.

Figure 16 (a) presents the dependence of  $C_D$  on  $\xi$ , which shows clearly that  $C_D$  and  $\xi$  are almost linearly related for the circular cylinder in the absence of the transition and the polygons of  $N \leq 8$ . The data may be least-square-fitted to the following straight lines:

$$C_D = 0.0128\xi + 0.9, \quad \text{for } Re = (2.0 \sim 10.0) \times 10^4. \quad (3.9)$$

Figure 16 (b) combines three  $Re$  cases and both NC and NF orientations. The data for

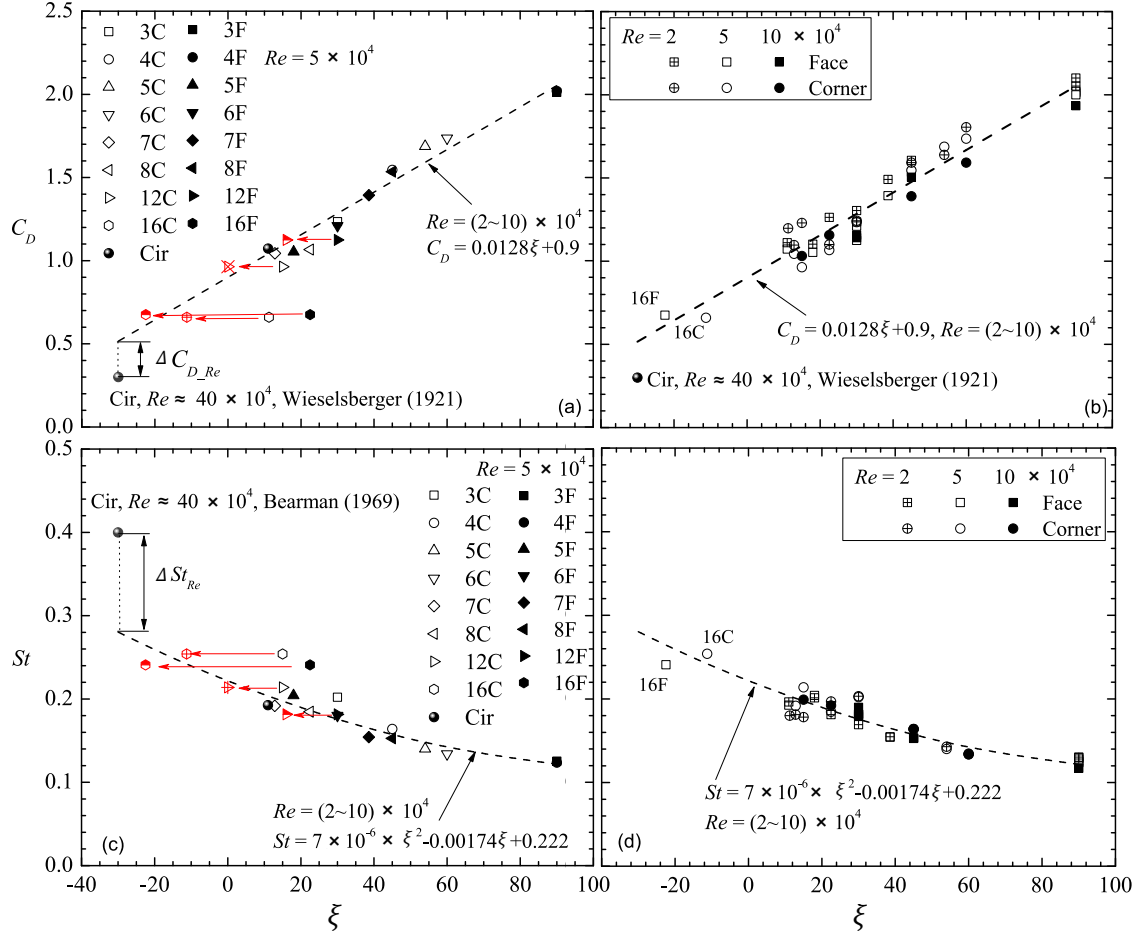


FIGURE 16. Dependence on  $\xi$  of (a)  $C_D$  at  $Re = 5.0 \times 10^4$ ; (b)  $C_D$  at  $Re = 2.0 \times 10^4, 5.0 \times 10^4, 10.0 \times 10^4$ ; (c)  $St$  at  $Re = 5.0 \times 10^4$ ; (d)  $St$  at  $Re = 2.0 \times 10^4, 5.0 \times 10^4, 10.0 \times 10^4$ . The dashed lines are the least-square-fitted to the data of the circular cylinder and  $N \leq 8$  in (b) and (d), where no transition takes place. The data obtained in the wake of a circular cylinder at  $Re = 40.0 \times 10^4$  from Wieselsberger (1921) and Bearman (1969) are also included for comparison. The left-pointing arrows in (a) and (c) illustrate the effects of the transition on the estimate of  $\xi$ , that is,  $\xi$  changes from the black colour symbol to the red once the transition occurs.

$Re = 1.0 \times 10^4$  were obtained in the wake of the polygons of  $D = 50\text{mm}$ . Evidently, the linear relation remains valid for all the data. The empirical correlation equation 3.9 does not take the effect of  $Re$  into account, that is,  $\xi$  remains the same for a given polygon in the subcritical regime and so does  $C_D$ . In fact,  $C_D$  for most polygons subtly decreases as  $Re$  increases, which could be considered in equation 3.9 by including a  $Re$ -related correction factor. However, this correlation term is found to be very small compared to the  $\xi$  term, essentially within the uncertainty of equation 3.9. For example,  $C_D$  reduces by  $\approx 10\%$  as  $Re$  changes from  $2.0 \times 10^4$  to  $1.0 \times 10^5$ . Therefore, the  $Re$  correction is dropped.

Figure 16 (a) also reflects the importance of determining the true  $\xi$  for the case when the transition takes place, as indicated by the left-pointing arrows. Apparently, if  $\xi$  in the subcritical regime is used for that in the critical regime, the data points will deviate further from the fitting curve. Taking the  $N = 16$  polygon for example, the transition

incurs a change in  $\xi$  from  $11.25^\circ$  to  $-11.25^\circ$  for 16C and from  $22.5^\circ$  to  $-22.5^\circ$  for 16F. Once the correct  $\xi$  is used, the corresponding  $C_D$  collapses onto the fitting curves reasonably well, as illustrated in figure 16 (b), that is, equation 3.9 may also apply to cases in the critical regime, as long as the correct  $\xi$  is used. This implies that equation 3.9 can be used to predict the true separation point location and the separation angle for polygons given the flow regime.

The data from Wieselsberger (1921) for a circular cylinder in the critical flow regime ( $Re = 4.0 \times 10^5$ ) is also included for comparison, which deviates significantly from the fitting curve. This is not unexpected since the  $Re$  of the data is beyond the  $Re$  range over which the correlation is obtained.

The  $St$  data corresponding to  $C_D$  shown in figure 16 (a-b) are presented in figure 16 (c-d). It is obvious that the  $St$ - $\xi$  correlation is not quite linear and the data are least-square-fitted to a second-order polynomial, viz.

$$St = 7 \times 10^{-6} \xi^2 - 0.00174 \xi + 0.222, \quad \text{for } Re = (2.0 \sim 10.0) \times 10^4. \quad (3.10)$$

As shown in figure 16 (c), the data collapse quite well onto this fitting curve when the correct  $\xi$  is used. Compared to  $C_D$ , the variation in  $St$  with  $Re$  is even smaller, within  $\pm 4\%$ . Thus the  $Re$  correction factor is also not necessary.

Equations 3.9 and 3.10 may be used to estimate  $C_D$  and  $St$  of the untested cases. Take 10C case for example. In the subcritical regime,  $\xi(10C)$  can be calculated from equation 3.8 to be  $36^\circ$ . By substituting  $\xi(10C)$  into equations 3.9 and 3.10, we obtain  $C_D(10C) \approx 1.36$  and  $St(10C) \approx 0.168$ , which agree very well with the predictions in § 3.2 (figure 6).

### 3.5. Relation between $C_D$ and $St$

The empirical relations of equations 3.9 and 3.10 could be combined to connect directly  $C_D$  and  $St$ , although additional uncertainties may be induced as some data deviate from the fitting curves more than the others. As such, we fit, based on the least squares technique, all the data from the measurements directly to the correlation form proposed by Hoerner (1965), viz.

$$\zeta = C_D^{0.6} St, \quad (3.11)$$

where  $\zeta$  is a constant. Figure 17 indicates that  $\zeta = 0.2$  appears to be the best fit to all the tested polygons and the  $Re$  range ( $1.0 \times 10^4 \sim 6.0 \times 10^4$ ). The upper and lower envelopes, given by  $\zeta = 0.22$  and  $0.18$  enclose most of the data points except 2F, 3C and some 4C data which occur above the upper envelope. A common feature for 2F and 3C polygons is the lack of leeward body volume or after-body, leading to a higher back pressure coefficient and hence a larger  $C_D \cdot St$  value (Bearman 1967). Using equation 3.11 to calculate  $C_D$  from  $St$  or vice versa yields a maximum error of about  $\pm 10\%$ . This error may be further reduced by fine tuning the  $\zeta$  value. For example, letting  $\zeta$  to be 0.23 will enclose most of the 2F and 3C data inside the envelopes.

A number of empirical  $C_D \sim St$  relations proposed by previous researchers are also plotted in figure 17 for the purpose of comparison, i.e.

$$0.21 = C_D^{0.75} St, \quad \text{Hoerner (1965)} \quad (3.12)$$

$$k = 2^{11/2} \pi \frac{C_D St}{C_D + 1}, \quad \text{Ahlborn et al. (2002)} \quad (3.13)$$

$$0.23 = C_D St, \quad \text{Alam & Zhou (2008),} \quad (3.14)$$

where  $k$  is an energy parameter which varies in general with different bluffbody shapes. Almost all the present data including the two envelopes ( $\zeta = 0.22, 0.18$ ) fall between the



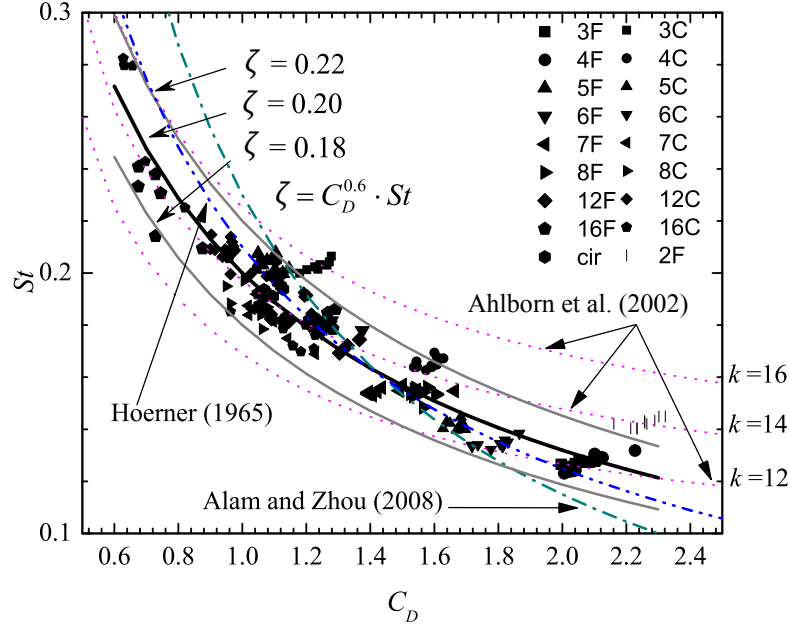


FIGURE 17. Empirical relation between  $St$  and  $C_D$  for all the cases tested at  $Re = (1.0 \sim 6.0) \times 10^4$ .  $\zeta = C_D^{0.6} St = 0.2$  is the fitting curve based on the least squares technique, with  $\zeta = 0.22$  and  $0.18$  corresponding to the upper and the lower envelopes, respectively. Correlations by Hoerner (1965), Ahlborn *et al.* (2002) and Alam & Zhou (2008) are also included for the purpose of comparison.

two curves corresponding to  $k = 12$  and  $16$ , respectively, of equation 3.13. Equation 3.12 does not seem to represent the present data very well for  $C_D < 1$ . Equation 3.14 exhibits a deviation from the data for  $C_D < 1$  and  $C_D > 2$  because this equation is derived based on the assumption of energy conservation in spite of inevitable energy exchange between the cylinder and the supporting frames in actual experiments.

It is worth making a comparison between presently proposed equation 3.11 and equations 3.12 ~ 3.14 based on a collection of data in the literature. Take  $N = 4$  and  $N = \infty$  for example to estimate  $St$  from  $C_D$  and vice versa. The results are given in figure 18. In figure 18 (a) the  $C_D$  data of a circular cylinder summarised in Tropea *et al.* (2007) is used to calculate the corresponding  $St$  from equations 3.12 ~ 3.14. In view of the data distribution for a circular cylinder in figure 17, the  $\zeta$  value in equation 3.11 is chosen to be  $0.21$  to represent the best  $C_D$  on the circular cylinder in figure 18 (a). The  $k$  value in equation 3.13 is chosen to be  $14.5$ , which gives the best fit. Note that Ahlborn *et al.* (2002) suggested  $k = 12.7$ , which produces a larger deviation to the experimental data. Equation 3.11, albeit obtained from the data over a limited  $Re$  range, gives the best fit to the experimental data from Tropea *et al.* (2007) for a wider  $Re$  range and is even in agreement with the data of  $Re > Re_c$ . Comparing to equation 3.12, equation 3.11 is equally good for  $Re < Re_c$  but better for  $Re > Re_c$ . Equation 3.14 displays a large deviation for  $10^3 < Re < 10^4$  and equation 3.13 agrees well with the experimental data for the entire  $Re$  range presented, similarly to equation 3.11.

Figure 18 (b) presents the  $C_D$  data for the  $N = 4$  polygon, calculated based on equations 3.11 to 3.14, from  $St$  summarised in Blevins (1990). Comparison is further made between the calculated  $C_D$  values and those reported in the literature. The  $\zeta$  value in 3.11 is chosen to be  $0.19$ . In equation 3.13,  $k$  is set to be  $12$ , which leads to a better fit



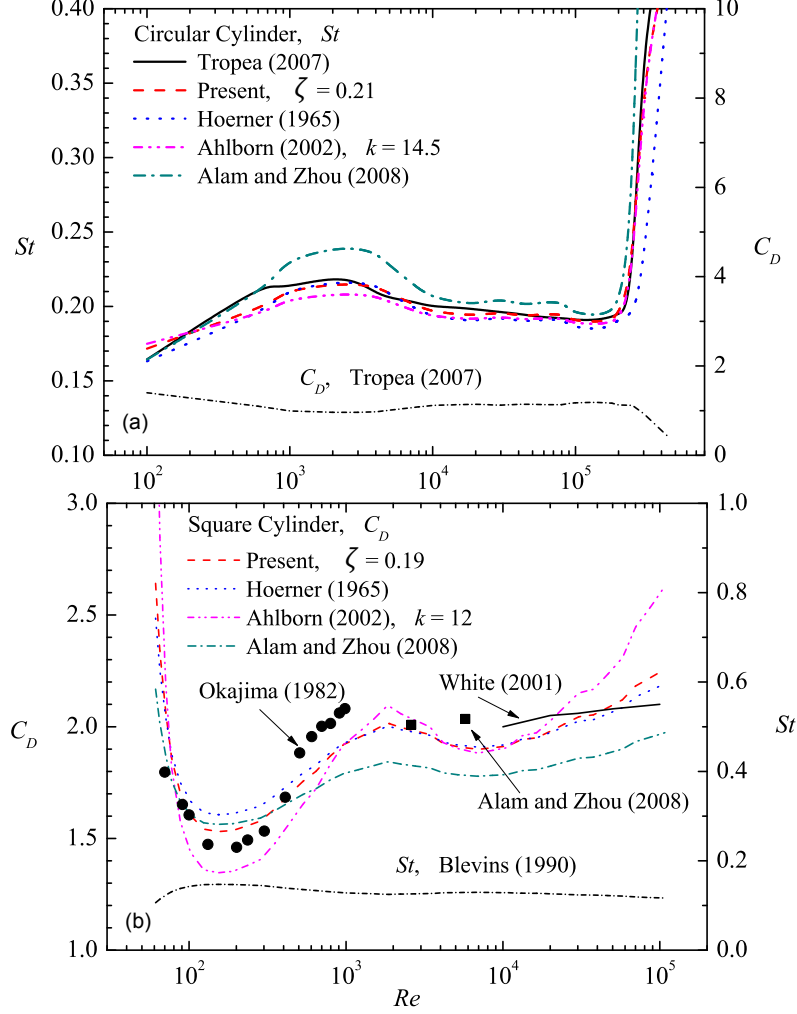


FIGURE 18. Evaluation of various  $St \sim C_D$  relations (equation 3.11 to 3.14): (a)  $St$  calculated from  $C_D$  on a circular cylinder summarised in Tropea *et al.* (2007); (b)  $C_D$  calculated from  $St$  on a square cylinder summarised in Blevins (1990). Experimental data from Okajima (1982), White (2001) and Alam & Zhou (2008) are included for the purpose of comparison.

to the data than  $k = 11.5$  proposed in Ahlborn *et al.* (2002). The  $C_D$  data calculated from equation 3.11 agree qualitatively with the available experimental data in Okajima (1982) for  $Re < 1.0 \times 10^3$ , but increase from 1.9 to 2.2 for  $1.0 \times 10^4 < Re < 1.0 \times 10^5$ , exceeding the experimental data reported in White (2001), with the largest deviation up to 10%. Assessment cannot be made for other  $Re$  ranges due to a lack of experimental data. The prediction from equation 3.12 is quite similar to that from equation 3.11.

Table 2 summarises  $C_D$  and  $St$ , reported in the literature, for the two-dimensional bodies of various cross-sectional geometry or irregular bluff bodies. The  $\zeta$  value is calculated based on  $C_D$  and  $St$  from equation 3.11. While most bluff bodies fall in between the envelopes ( $0.18 \leq \zeta \leq 0.22$ ),  $\zeta$  tends to be small for more streamline-shaped bodies. For example, the rectangular cylinder with an aspect ratio 2:1 corresponds to  $\zeta = 0.11$ , smaller than 0.24, with an aspect ratio of 1:2. Table 2 and also figure 18 indicate that  $\zeta$  is independent of  $Re$  for cylinders with mild bluffness, at least for the  $Re$  range examined

Prototype	Re	$C_D$	St	$\zeta$	Data source
Rectangular cylinder (2:1)	$\approx 10^4$	1.80	0.080	0.11	Tropea <i>et al.</i> (2007)
Rectangular cylinder (1:2)		2.40	0.140	0.24	
Semi-circular cylinder (CW)		1.20	0.210	0.23	
Semi-circular cylinder (FW)		1.70	0.160	0.22	
Half tube (CW)		1.20	0.210	0.23	
Half tube (CL)		2.30	0.130	0.21	
The Great Belt East Bridge	$2 \times 10^6$ $5 \times 10^4$	0.60 0.68	0.220 0.180	0.16 0.14	Schewe & Larsen (1998)
Square cylinder	2600	2.00	0.128	0.19	Alam & Zhou (2008)
RC square cylinder ( $r/d = 0.157$ )		1.70	0.150	0.21	
RC square cylinder ( $r/d = 0.236$ )		1.45	0.180	0.22	
RC square cylinder ( $r/d = 0.157$ )		1.20	0.210	0.23	
CC square cylinder $c/d = 0.100$	$6 \times 10^4$	1.23	0.150	0.17	Yamagishi <i>et al.</i> (2010)
CC square cylinder $c/d = 0.167$		1.60	0.155	0.21	

TABLE 2. The  $C_D$  and St values of various irregular polygon cylinders reported in the literature and their correlation coefficient  $\zeta$  calculated from equation 3.11. In the table, CW, FW and CL denote the windward-facing curved surface, the windward-facing flat surface and the leeward-facing curved surface, respectively; RC and CC represent the rounded corner and the chamfered corner, respectively;  $r$ ,  $d$  and  $c$  are the abbreviations for the radius of the rounded corner, the side length of the square cylinder and the size of the chamfered corner, respectively.

presently. Furthermore, the experimental data (not shown) confirm that  $\zeta$  changes in the range of  $0.20 \pm 0.02$  as the angle of attack of the polygon cylinder varying between the corner and the face orientations at  $\text{Re} = 5.0 \times 10^4$ .

Figure 17 indicates that St and  $C_D$  are inversely related. This can be demonstrated analytically.

Assuming that the vortices shed from the cylinders are two-dimensional and can be approximately described by the Lamb-Oseen vortex model (Saffman 1995), the azimuthal velocity  $u_\theta$  of an isolated vortex can be written as:

$$u_\theta(r_s, t) = \frac{\Gamma_o}{2\pi r_s} \left[ 1 - \exp\left(-\frac{r_s^2}{4\nu t}\right) \right], \quad (3.15)$$

where  $t$  is time ( $\sqrt{4\nu t}$  is the characteristic vortex size),  $\Gamma_o$  is the vortex strength and  $r_s$  is the radius to the vortex centre. The kinetic energy of the flow field associated with an isolated Lamb-Oseen vortex may be written as:

$$\begin{aligned} \text{KE} &= \int_0^\infty \rho \pi r_s u_\theta^2 dr_s \\ &= \rho \frac{\Gamma_o^2}{4\pi} \int_0^\infty \frac{1}{r_s} \left[ 1 - 2\exp\left(-\frac{r_s^2}{4\nu t}\right) + \exp\left(-\frac{2r_s^2}{4\nu t}\right) \right] dr_s, \end{aligned} \quad (3.16)$$

where  $\rho$  is the fluid density. From the energy budget point of view, one pair of vortices form over one period of vortex shedding, which produces a drag force  $F_D$ , i.e.  $KE = F_D U_\infty \tau$ , where  $\tau = D/U_\infty$  is the characteristic time scale of vortex shedding. Defining a dimensionless circulation  $K = \Gamma_o/\pi U_\infty D$  and writing the integral in equation 3.16 as

$\eta(t)$ ,  $C_D$  is then related to St as:

$$C_D = \pi K^2 \text{St} \eta(t). \quad (3.17)$$

The formation of a vortex is the roll-up of a shear layer, and vortex shedding occurs when fluid engulfed in carrying vorticity with opposite signs cuts off further the entrainment of circulation (Gerrard 1966). Taking the average velocity in the boundary layer to be  $U_\infty/2$  and  $\delta$  to be the characteristic boundary layer thickness, consider a shear layer with vorticity  $\omega \sim U_\infty/\delta$  rolling-up over time  $\tau$ . Then

$$K \sim \frac{1}{\pi D U_\infty} \left( \frac{U_\infty}{\delta} \right) (\delta \tau U_\infty / 2) = \left( \frac{1}{2\pi} \right) \text{St}^{-1}. \quad (3.18)$$

Note that, depending on the degree of bluffness and hence the wake width, only a fraction of the circulation contributes to the vortex formation (Bearman 1984). Equation 3.18 then needs to be revised such that

$$K \sim \frac{1}{\pi D U_\infty} \left( \frac{U_\infty}{\delta} \right) (\delta \tau U_\infty / 2) f(D_w^*) = \frac{f(D_w^*)}{2\pi} \text{St}^{-1}, \quad (3.19)$$

The Re effect may be reflected in  $D_w^*$ . Substituting equation 3.19 into 3.17 yields

$$C_D = \frac{1}{4\pi \text{St}} f(D_w^*) \eta(t). \quad (3.20)$$

The integrand of  $\eta(t)$  is bounded over  $r_s \in [0, \infty)$  and the integral  $\eta(t)$  is not very sensitive to  $t$ . Therefore,  $\eta(t)$  is a weak function of the characteristic vortex size  $\sqrt{4\nu t}$ . Taking a realistic vortex size to be in the order of  $D/2$ ,  $\eta$  is typically around 7.0. Substituting the known numerical values into  $f$ , we may finally obtain

$$C_D = f(D_w^*) \text{St}^{-1}. \quad (3.21)$$

As the empirical correlation 3.11 agrees well with the present experimental data, we may infer  $f(D_w^*) \sim \zeta C_D^{-0.4}$ . Note that  $C_D$  is an increasing function of  $D_w^*$ , that is,  $C_D$  increases with larger  $D_w^*$ . Using the  $D_w^*$  data at  $\text{Re} = 1.0 \times 10^4$  shown in figure 9 and the corresponding  $C_D$ , we may find  $D_w^* \sim C_D^{0.8}$ . Therefore,  $f(D_w^*) \sim (D_w^*)^{-1/2}$ .

#### 4. Concluding remarks

The aerodynamic characteristics of polygon cylinders ( $N = 2, 3 \sim 8, 12, 16, \infty$ ) are systematically studied over a Re range of  $1.0 \times 10^4 \sim 1.0 \times 10^5$ , based on the three-dimensional force transducer, smoke flow visualisation and PIV measurements. Both corner and face orientations of the polygon cylinders are examined. Following conclusions may be drawn out of this work.

It has been found that  $C_D$ ,  $C_L'$  and St all vary with N as well as with the polygon orientation. The dependence of  $C_D$  on N exhibits a distorted Cartesian pattern (figure 6 a-b). So does that of St on N (figure 6 c-d). This pattern may be used to predict  $C_D$  and St for untested polygons, e.g.  $N = 9 \sim 11$ . In general,  $C_D$ ,  $C_L'$  and St all depend on the polygon orientation. This dependence however contracts with increasing N. While  $C_L'$  becomes independent of the polygon orientation for  $N \geq 12$ ,  $C_D$  and St may differ, albeit very slightly, from one polygon orientation to the other. The characteristic length scales of the wake, such as the wake width and the length of the reversed flow region, and their dependence on N are also documented.

The present flow visualisation data (figure 11) shows unequivocally that, given polygons of  $N \leq 8$ , the flow separation point is fixed at the corner of the maximum width

point  $T_o$ . As such,  $C_D$  and  $St$  change little, essentially independently of  $Re$  (see also figure 4). In a few cases, e.g. 5F and 7C, although separating at corner  $T_1$ , upstream of  $T_o$ , the flow reattaches near  $T_o$ , again resulting in  $C_D$  and  $St$  that are independent of  $Re$ . The cylinders of N12 and N16 undergo the transition at  $Re_c \approx 2.4 \times 10^4$  and  $\approx 3.4 \times 10^4$ , respectively; correspondingly,  $C_D$  drops substantially, accompanied by a large increase in  $St$ . Once the transition takes place, the flow separation is postponed, allowing more recovery in pressure; the energised boundary layer due to the transition enhances the shear layer instability, causing relatively small-scale vortices to be generated at higher frequencies.

One of the most important findings of this study is the corrected flow separation angle  $\xi$ , which has essentially taken the separation-reattachment phenomenon into account. This angle is uniquely dependent on the orientation and  $N$  of the polygon in the sub-critical regime (figure 15), i.e.  $Re < Re_c$ . More importantly, the dependence of  $C_D$  or  $St$ , which is greatly scattered if plotted against  $N$  (figure 6) or other parameters, on  $\xi$  collapses onto a single curve as shown in figure 16, even under the circumstance of the transition, implying that  $\xi$  is a scaling factor for both  $C_D$  and  $St$ . The correlation between  $C_D$  and  $\xi$  is even linear. This finding allows us to predict the  $C_D$  and  $St$  of the polygon cylinder from  $\xi$  from a careful flow visualisation experiment, without the need for the force transducer of high dynamic response or hotwires. The linear correlation between  $\xi$  and  $C_D$  is perhaps not surprising. Ahlborn *et al.* (2002) showed that  $C_D$  is linearly proportional to  $\tan \theta$ , where  $\theta$  is the angle between the transverse velocity and the streamwise velocity of vortices separated from the cylinder. Yeung (2009) found a linear relation between  $C_D$  and  $(C_p)_b$  for some bluff bodies such as cones and spheres. The definition of  $\xi$  is essentially related to  $\theta$  and  $(C_p)_b$  on the polygon; once the transition takes place,  $\xi$  characterises uniquely the location of the flow separation point. If the direction of  $U_s$  (see § 3.3, related to the geometry of the polygon) is considered,  $\theta_s$  and hence  $(C_p)_b$  can be inferred from  $\xi$ .

It has been found that  $Re_c$  rises for larger  $N$  given  $N \geq 12$  (figure 5 a). An analogy, in terms of  $Re_c$ , between the polygons of  $N \geq 12$  and the rough surface circular cylinders is proposed. The corners of these polygons act like the roughness elements, with a height  $\varepsilon$  calculated by equation 3.1, evenly distributed on the surface of a smooth circular cylinder. The dependence of  $Re_c$  on  $\varepsilon/D$  follows well both qualitatively and quantitatively the dependence of  $Re_c$  on the relative roughness of a roughened circular cylinder (figure 5). As a result,  $Re_c$  for the untested polygons of large  $N$  may be predicted from the well documented  $Re_c$  of the rough surface circular cylinder. However, for  $N < 12$ , the size and number of ‘the roughness elements’ become relatively large and small, respectively, and the corners cannot be treated as roughness elements anymore and the analogy is no longer valid.

The one-to-one correlation between  $C_D$  and  $\xi$  and that between  $St$  and  $\xi$  imply a relation between  $C_D$  and  $St$ . A new empirical correlation is proposed, i.e.  $\zeta = C_D^{0.6} St$ , and the best fit to the present experimental data as well as those in the literature is  $\zeta = 0.20$ . When  $\zeta = 0.22$  and  $\zeta = 0.18$ , the corresponding curves form two envelopes that enclose most of the available experimental data points. This relationship is found to be valid not only for the polygon cylinders but also the bluff bodies of irregular cross-section over  $Re = 50 \sim 10^6$ .

Finally, we have demonstrated analytically that  $C_D$  and  $St$  are inversely related, as shown by the experimental data in figure 17.

## 5. Acknowledgement

S. J. Xu wishes to acknowledge the support from NSFC through grants 10972118 and 11472158. L. Gan would like to thank the support from the United Kingdom Royal Society of Engineering Newton Research Collaboration Fund (NRCP/1415/130). Y. Zhou is grateful for the financial support from NSFC through grant 51421063 and from Scientific Research Fund of Shenzhen Government through grant KQCX20140521144301394. The authors also acknowledge Prof. Z. N. Wu of Tsinghua University for his constructive discussions.

## REFERENCES

- AHLBORN, B., SETO, M. L., & NOACK, B. R. 2002 On drag, Strouhal number and vortex-street structure. *Fluid Dyn. Res.* **30**, 379–399
- ALAM, M. M. & ZHOU, Y. 2007 Turbulent wake of an inclined cylinder with water running. *J. Fluid Mech.* **589**, 261–303
- ALAM, M. M. & ZHOU, Y. 2008 Alternative drag coefficient in the wake of an isolated bluff body. *Phys. Rev. E* **78**, 036320
- ANTONIA, R. A. & RAJAGOPALAN, S. 1990 Determination of drag of a circular cylinder. *AIAA journal* **28**(10), 1833–1834
- BEARMAN, P. 1967 On vortex street wakes. *J. Fluid Mech.* **28**, 625–641
- BEARMAN, P. W. 1969 On vortex shedding from a circular cylinder in the critical Reynolds number regime. *J. Fluid Mech.* **37**, 577–585
- BEARMAN, P. W. 1984 Vortex Shedding from Oscillating Bluff Bodies. *Annu. Rev. Fluid Mech.* **16**, 195–222
- BLEVINS, B. D. 1990 Flow-induced vibration, 2nd edition. *New York, Van Nostrand Reinhold*, 50
- BOSCH, H. R. & GUTERRES, R. M. 2001 Wind tunnel experimental investigation on tapered cylinders for highway support structures. *J. Wind Engng Ind. Aerodyn.* **89**, 1311–1323
- COWDREY, C. F. 1962 A note on the use of end plates to prevent three dimensional flow at the ends of bluff bodies. *NPL Aero Rep.* 1025
- DENIZ, S. & STAUBLI, T. H. 1997 Oscillating rectangular and octagonal profiles: interaction of leading- and trailing-edge vortex formation. *J. Fluids Struct.* **11**, 3–31
- GERICH, D. & ECHELMANN, H. 1982 Influence of end plates and free ends on the shedding frequency of circular cylinders. *J. Fluid Mech.* **122**, 109–121
- GERRARD, J. H. 1966 The mechanics of the formation region of vortices behind bluff bodies. *J. Fluid Mech.* **25**(02), 401–413
- GÜVEN, O., FARELL, C. & PATEL, V. C. 1980 Surface-roughness effects on the mean flow past circular cylinders. *J. Fluid Mech.* **98**(4), 673–701
- HOERNER, S. F. Fluid-Dynamic Drag, Hoerner Fluid Dynamics. *Bricktown New Jersey*. O-1 – Z-8
- KHALEDI, H. A. & ANDERSSON H. I. 2011 On vortex shedding from a hexagonal cylinder. *Phy. Let. A* **375**, 4007–4021.
- MATSUMOTO, M. 1999 Vortex shedding of bluff bodies: A Review. *J. Fluids Struct.* **13**, 791–811
- MILLS, R., SHERIDAN, J. & HOURIGAN, K. 2003 Particle image velocimetry and visualization of natural and forced flow around rectangular cylinders. *J. Fluid Mech.* **478**, 299–323
- NORBERG, C. 1994 An experimental investigation of the flow around a circular cylinder: influence of aspect ratio. *J. Fluid Mech.* **258**, 287–316
- NORBERG, C. 2003 Fluctuating lift on a circular cylinder: review and new measurements. *J. Fluids Struct.* **17**, 57–96
- OKAJIMA, A. 1982 Strouhal numbers of rectangular cylinders. *J. Fluid Mech.* **123**, 379–398
- PONTA, F. L. 2006 Effect of shear-layer thickness on the Strouhal Reynolds number relationship for bluff-body wakes. *J. Fluids Struct.* **22**, 1133–1138
- ROSHKO, A. 1955 On the wake and drag of bluff bodies. *J. Aeronaut. Sci.* **22**, 124–132
- SAFFMAN, P. G. 1995 Vortex dynamics. *Cambridge University Press*

- SCHEWE, G. & LARSEN, A. 1988 Reynolds number effects in the flow around a bluff bridge deck cross section. *J. Wind Engng Ind. Aerodyn.* **74**, 829–838
- SKEWS, B. W. 1991 Autorotation of many-sided bodies in an airstream. *Nature* **352**, 512–513
- SKEWS, B. W. 1998 Autorotation of polygonal prisms with an upstream vane. *J. Wind Engng Ind. Aerodyn.* **73**, 145–158
- SRIGRAROM, S. & KOH, A. K. G. 2008 Flow field of self-excited rotationally oscillating equilateral triangular cylinder. *J. Fluids Struct.* **24**, 750–755
- SZEPESSY, S. & BEARMAN, P. W. 1992 Aspect ratio and end plate effects on vortex shedding from a circular cylinder. *J. Fluid Mech.* **234**, 191–217
- THOMPSON, M. C., LEWEKE, T. & WILLIAMSON, C. H. K. 2001 The physical mechanism of transition in bluff body wake. *J. Fluids Struct.* **15**, 607–616
- TIAN, X. & LI, S. 2007 Scientific measurements of disturbance on the prototype stands in a low speed wind tunnel. *Experimental research in aerodynamics* **25(3)**, 1–6 in Chinese
- TIAN, Z. W. & WU, Z. N. 2009 A study of two-dimensional flow past regular polygons via conformal mapping. *J. Fluid Mech.* **628**, 121–154
- TROPEA, C., YARIN, A. & FOSS, J. F. (EDS.) 2007 Springer Handbook of Experimental Fluid Mechanics. *Springer-Verlag Berlin Heidelberg*, 1125–1145
- VICKERY, B. J. 1966 Fluctuating lift and drag on a long cylinder of square cross-section in a smooth and in a turbulent stream. *J. Fluid Mech.* **25**, 481–494
- WEST, G. S. & APELT, C. J. 1982 The effects of tunnel blockage and aspect ratio on the mean flow past a circular cylinder with Reynolds numbers between 104 and 105. *J. Fluid Mech.* **114**, 361–377
- WIESELSBERGER, C. 1982 Recent statements on the laws of liquid and air resistency. *Phys. Z.* **22**, 321
- WILLIAMSON, C. H. K. 1988 Defining a universal and continuous Strouhal-Reynolds number relationship for the laminar vortex shedding of a circular cylinder. *Phys. Fluids* **31(10)**, 2742–2744
- WILLIAMSON, C. H. K. 1996 Vortex dynamics in the cylinder wake. *Annu. Rev. Fluid Mech.* **28**, 477–539
- WILLIAMSON, C. H. K. & BROWN, G. L. 1998 A series in  $1/\sqrt{Re}$  to represent the Strouhal-Reynolds number relationship for the cylinder wake. *J. Fluid Struct.* **12(8)**, 1073–1085
- WHITE, F. W. 2001 Physics - Fluid Mechanics, 4th edition, *McGraw-Hill*, 277–311; 427–476
- YAMAGISHI, Y., KIMURA, S. & MAKOTO, O. 2010 Flow characteristics around a square cylinder with changing chamfer dimensions. *J. Visual.* **13(1)**, 61–68
- YEUNG, W. W. H. 2009 On pressure invariance, wake width and drag prediction of a bluff body in confined flow. *J. Fluid Mech.* **622**, 321–344
- YEUNG, W. W. H. 2010 On the relationships among Strouhal Number, pressure drag, and separation pressure for blocked bluff-body flow. *J. Fluids Engng.* **132(2)**, 021201
- ZDRAVKOVICH, M. M. 1997 Flow around circular cylinders, vol. 1, *Oxford University Press*, Oxford